Responses of tidal modification and nonlinearity to large-scale sequential harbor constructions in the northeastern China

Accepted Manuscript

Responses of tidal modification and nonlinearity to large-scale sequential harbor constructions in the northeastern China

Cuiping Kuang, Honglin Song, Jie Gu, Qingping Zou, Huidi Liang, Xiaoming Sun, Zhen Ma

PII: S0278-4343(19)30161-X

DOI: https://doi.org/10.1016/j.csr.2019.06.001

Reference: CSR 3931

To appear in: *Continental Shelf Research*

Received Date: 2 April 2019

Revised Date: 3 June 2019

Accepted Date: 6 June 2019

Please cite this article as: Kuang, C., Song, H., Gu, J., Zou, Q., Liang, H., Sun, X., Ma, Z., Responses of tidal modification and nonlinearity to large-scale sequential harbor constructions in the northeastern China, *Continental Shelf Research* (2019), doi: https://doi.org/10.1016/j.csr.2019.06.001.

Responses of tidal modification and nonlinearity to large-scale sequential harbor constructions in the northeastern China (revised version)

Cuiping Kuang [a], Honglin Song [a], Jie Gu [b], Qingping Zou[c], Huidi Liang [a], Xiaoming Sun[d] and Zhen Ma[d]

[a] Department of Hydraulic Engineering, College of Civil Engineering, Tongji University, Shanghai 200092, China

[b] College of Marine Ecology and Environment, Shanghai Ocean University, Shanghai 201306, China

[c] The Lyell Centre for Earth and Marine Science and Technology, Institute for Infrastructure and Environment, Heriot-Watt University, Edinburgh, EH14 4AS, UK

[d] Tianjin Institute of Geology and Mineral Resources, Tianjin 300170, China

Abstract

The impacts of large-scale coastal structures on tidal dynamics have been studied extensively over the past decades, but the relevant mechanisms are not fully understood. In this study, a two-dimensional Delft3D barotropic tidal model is applied to investigate the tidal dynamic changes induced by the large-scale sequential constructions of Huanghua-Binzhou Harbor in the northeastern China during year 2003-2016. It was found that the predominant M_2 tide is increased on the stoss side and decreased on the lee side of the harbor by 2-6 cm due to the harbor constructions. This feature is due to 1) the increased and decreased tidal energy on the stoss and lee side, respectively, by the harbor structures; 2) the structure-induced changes in momentum flux is balanced by pressure gradient, and thus leads to a larger tidal range on the stoss side and a smaller tidal range on the lee side. The sensitivity studies on nonlinear M_4 tide demonstrate that it is generated locally by M_2 self-self interaction, which is not only related to M_2 tidal energy but also nonlinearity. Consequently, M_4 tide increases towards the shore on the tidal flat with natural slope due to enhanced nonlinearity by decreasing water depth, but is proportional to M_2 tide on the tidal flat with a constant water depth, where local nonlinearity is nearly the same in space. In addition, the energy transfer from M_2 to M_4 is affected by the structure-induced changes in nonlinearity, resulting in different responses of M_2 and M_4 tide to the coastal structure.

Keywords: tidal dynamics; nonlinearity; tidal components; harbor constructions; numerical modelling; Bohai Bay

22

23 # 1 Introduction

24 Recent booming economy and population growth along the coast have led to rapid
25 expansion of industry, urbanization and infrastructure, therefore, unprecedented large-scale
26 anthropogenic interventions in coastal zone (Turner et al., 1996, Tian et al., 2016). This trend
27 will continue in the future and cause ecosystem degradation, loss of tidal flats and wetlands,
28 beach erosion and shoreline retreat (Cheong et al., 2013; Pelling et al., 2013. Tian et al., 2016;
29 Xu and Gong, 2018). In the past decades, much efforts have been dedicated to investigate the
30 impacts of coastal man-made structures and large-scale human interventions (Byun et al.,
31 2004; Gao et al., 2014; Gao et al., 2018; Guo et al., 2018; Li et al., 2012; Song et al., 2013;
32 Wang et al., 2014; Zarzuelo et al., 2015; Zhu et al., 2018). According to these studies, human
33 interventions may change the hydrodynamics and morphodynamics to various extent. For
34 example, land reclamation cuts off the link between sea and land and its impacts on local
35 tidal dynamics vary with the reclaimed scale, site location and tidal conditions (Bertin et al.,
36 2005; Gao et al., 2014; Liang et al., 2018). Moreover, land reclamation may modify the
37 patterns of suspended sediment transport and morphology because the sediment deposition is
38 hindered as the reclaimed land is separated from estuary and ocean (Gao et al., 2018; Liang et
39 al., 2018; Wang et al., 2012). Construction of jetty/dam may lead to tidal choking (Byun et al.,
40 2004) and affect the sedimentological process in coastal areas (Davis and Barnard, 2003;
41 Mulder and Louters, 1994; Dai et al., 2013, 2014, 2018). In the presence of dredging at the
42 entrance of bay, the deepening of channel has remarkable influence on the hydrodynamics
43 inside the bay (Blott et al., 2006; Zarzuelo et al., 2015) and can also stabilize the

channel-shoal system (Wang et al., 2014). Under the combined action of multiple engineering projects in the same region, the geometrical changes generated by reclamations and jetties have great impact on the redistribution of tidal energy around a harbor in deep sea (Guo et al., 2018), but have limited influence on the shift of channels in the coast (Wang et al., 2014).

In the past, it was feasible to estimate the impact of individual coastal structure or project separately (Feng et al., 2008; Lu et al., 2009; Li et al., 2010) because of their limited size and influence on the surrounding water. Nowadays, however, the size and density of the anthropogenic intervention project has increased dramatically, especially in the rapidly developing regions such as the Bohai Bay, northeast of China (Fig. 1). As a result, the interactions among coastal structures and projects are no longer negligible (Hou, 2013; Pelling, 2013; Zhu et al., 2018). It was noticed that multiple coastal structures could form an engineering cluster and its long artificial coastline can lead to a rise in local tidal amplitude (Hou, 2013; Pelling et al., 2013; Song et al., 2013), which in turn increases the risk of disasters during extreme weather due to the loss of natural buffers (Arkema et al., 2013; Crain et al., 2009; Ding and Wei, 2017). Bohai Bay accounts for about 24.5% of domestic reclamation area in China between year 1985 and 2010 (Tian et al., 2016) by constructing Caofeidian Harbor, Tianjin Harbor and Huanghua-Binzhou Harbor (Fig. 1c). Hou (2013) examined the cumulative impact of sequential harbor constructions in the Bohai Bay and found that the three harbor “clusters” increase coastal tidal range and affect the position of M_2 amphidromic point since 2003. Hou (2013) also found that the combined effect of the harbors is much more than a linear superposition of each harbor. It has been noted that the impacts of these coastal structures could extend to nearly the entire Bohai Bay (Hou, 2013),

but would be confined in the bay as the local tidal dynamics is primarily influenced by the tides from the Yellow Sea offshore (Pelling et al., 2013). The study area of the Huanghua-Binzhou Harbor lies in southwest Bohai Bay which is a silt-muddy coast suffered severe sediment siltation in windy days (Feng et al., 2008; Kuang et al., 2015). In order to relieve sediment siltation and improve harbor capacity, two 10.5 km-long regulation jetties were built in Huanghua Harbor during year 2004-2005 (Fig. 1d). Then, large-scale constructions of Huanghua Harbor began in 2009 and have reclaimed land over 75.6 km^2 (include waters enclosed by jetties) and consist the longest jetty of 32.8 km until 2016. In Binzhou Harbor, two jetties were built in 1997 to maintain the depth of waterway to its inland harbor. The coastal harbor of Binzhou Harbor was built on its existed western jetty from 2010 and was constructed in an even faster pace compared to Huanghua Harbor, with 36.6 km^2 land reclamation and 16.4 km jetty construction finished in just four years (2013-2016) (Fig. 1d). Consequently, the distance between Huanghua and Binzhou harbors has been reduced to 14.6 km in 2016, which is only half of their longest jetty, so the interaction and sheltering effects of these two harbors is no longer negligible, which is one of the motivation of this study.

Semidiurnal M_2 tide and its overtide M_4 are the main contributors to tidal asymmetry in the coastal area (Song et al., 2016a). Therefore, these two tidal constituents are often used to evaluate the impacts of coastal structures and projects in East China Sea (Gao et al., 2014; Guo et al., 2018; Li et al., 2017; 2018a, 2018b; Lefèvre et al., 2000; Pelling et al., 2013; Park et al., 2014; Song et al., 2013; Suh et al., 2014). The modification in M_2 tide by the "obstacles", e.g., coastal structures and islands, was found to be larger than that of diurnal

tides K_1 and O_1 and semidiurnal tide S_2 (Dai et al., 2017; Song et al., 2013; Wu et al., 2018). The relationship between M_2 tidal amplitude change and jetty/dyke layout has been investigated in Yangshan Harbor, East China (Guo et al., 2018), Taiwan Strait, Southeast China (Dai et al., 2017) and Saemangeum Dyke, West Korea (Lee et al., 2008; Suh et al., 2014; Park et al., 2014). These studies show that M_2 tidal amplitude has regular variation patterns around the structures, and Park et al. (2014) adopted a simple scaling argument to study this phenomena using momentum balance. Under the action of land reclamation, M_2 tidal wave is found to be distorted in the coast due to the modified geometrical funneling and frictional damping (Dyer, 1973) and shoaling (Li et al., 2012; 2018a; Gao et al., 2014). Moreover, the modification of tidal energy transport and redistribution due to coastline change are also examined to better understand the impacts of engineering project (Gao et al., 2014; Guo et al., 2018; Pelling et al., 2013; Song et al., 2013; Suh et al., 2014). It was found that the increased M_2 amplitude due to reclamation is mostly ascribed to the conversion of the tidal energy over the tidal flat into potential tidal energy (Song et al., 2013).

The nonlinearity for tides is one of our main concerns in this paper. Nonlinear physical processes associated with Navier-Stokes hydrodynamics can result in a distortion of tidal constituents (Gallagher and Munk, 1971; Parker, 1991). As tidal waves propagate into shallow water, tidal nonlinearity increases towards the coast and promotes the growth of overtides and compound tides through energy transfer from low to high frequency components, e.g. from M_2 to M_4 (Gallagher and Munk, 1971; Parker, 1991; Speer and Aubrey, 1985; Song et al., 2016a). The shallow-water tide M_4, a common quarter-diurnal constituents in M_2 dominated regions, is generated by the nonlinear terms of free surface in

the continuity equation, and advection and bottom friction in the momentum equations (Parker, 1991). The driving mechanism for M_4 tide is complicated since the dominant nonlinear term varies from one region to another (Zhu et al., 2017), depending on the geometry and bathymetry. According to the sensitivity study of M_4 by numerical modelling and theoretical analysis, the advection term is considered to be the main contributor to M_4 in Lunenburg Bay, Canada (Sheng and Wang, 2004), deep area of Zhitouyang Bay, China (Zhu et al., 2017) and Zhoushan Archipelago, China (Wu et al., 2018). Whereas, the bottom friction plays a more important role in generating M_4 tide in Jiaozhou Bay, China (Gao et al., 2014) and Xiangshan Bay, China (Li et al., 2018a). In addition, the nonlinear free surface term seems to dominate the M_4 generation in channels (Pingree and Maddock, 1978; Sheng and Wang, 2004). The response of M_4 tide to topography/bathymetry change (Gao et al., 2014; Li et al., 2018a; Liang et al., 2018) and tidal flat slope (Li et al., 2018a, 2018b) was found to be stronger than that of M_2 tide.

In summary, there is a lack of study of the mechanism underneath the changes of tidal energy and tidal amplitude due to coastal structures. In addition, the generation and variation of shallow-water tide M_4 in the Huanghua-Binzhou Harbor has not been previously reported or carefully examined based on energy transfer and nonlinearity. Hence, the objective of this study is 1) to estimate the impacts of sequential constructions of Huanghua-Binzhou Harbor on the local tidal dynamics during four construction phases; 2) to focus on the linkage between tidal characteristics and momentum terms, and also tidal energy, and tentatively pinpoint the physical mechanism of M_2 tidal distortion by coastal structures; 3) to further

131 understand the roles of energy transfer (from M_2 to M_4) and nonlinearity in the generation
132 and variation of local shallow-water tide M_4.

133 This paper is organized as follow: Section 2 gives a brief description of model setup and
134 validation. Section 3 provides the numerical model results of tidal dynamics changes by
135 harbor constructions. Section 4 discusses the jetty-induced changes of momentum terms and
136 their linkage with M_2 amplitude change, and examines the sensitivity of M_4 tide to tidal
137 forcing, bottom slope and nonlinearity. Finally, a conclusion is given in Section 5.
138

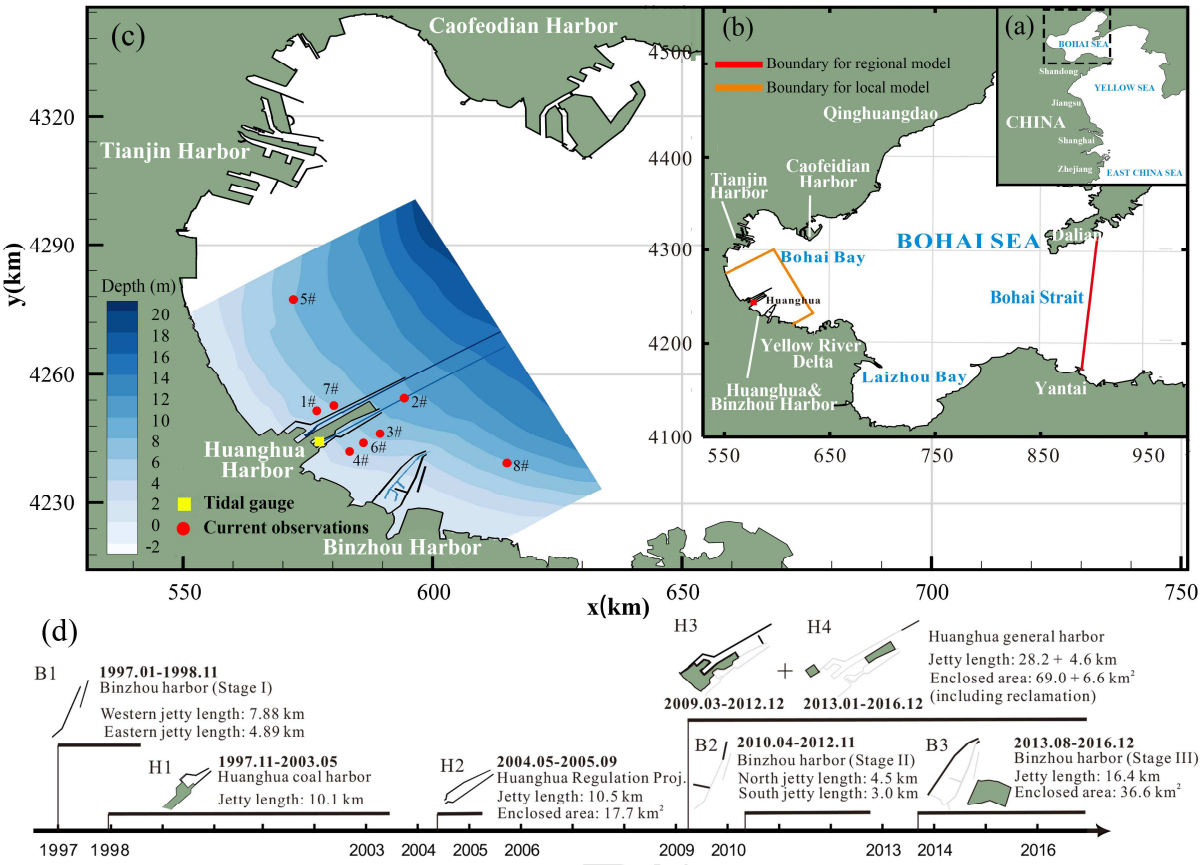

Fig. 1. (a) Geographical location of the study area as indicated by the dashed black line in. (b) Computational domain of the Bohai Sea regional model (with the offshore boundary in red) and the Huanghua-Binzhou Harbor local model (with three open boundaries in orange). (c) Spatial distribution of bathymetry (unit: m) with a coastline in year 2016 and the locations of tidal gauge (yellow rectangle) and current meters (red dots) used for model validation. (d) Timeline of the development of Huanghua-Binzhou Harbor from year 1997 to 2016. The coordinate system is based on the Gauss-Kruger projection with the central meridian at 117°E.

2 Model setup and validation

2.1 Model description

The tidal dynamics responses to sequential harbor constructions are investigated by the process-based model Delft3D, which has been proved to be a successful modeling system for simulating physical processes in coastal environments, in particular in long-term scales (Hu et al., 2009; Lee and Qu, 2004; Liang et al., 2018; van der Wegen and Roelvink, 2012; Vousdoukas et al., 2016; Zarzuelo et al., 2015). More importantly, the present tidal model set up by Delft3D-FLOW can be fully two-way coupled with other integrated models, e.g., Delft3D-SED and Delft3D-MOR, to further estimate the impacts of harbor construction on local sediment transport and morphological evolution in near future. Based on the Boussinesq and shallow water assumption, Delft3D-FLOW solves the unsteady shallow water equations on the Arakawa C-grid using an Alternating Direction Implicit (ADI) method and thus allows a fast and stable simulation. To reproduce the fluid motion in shallow water where the horizontal scale is significantly larger than vertical scale, the vertical momentum equation is reduced to the hydrostatic pressure relation as the vertical acceleration is negligible. The depth-averaged governing equations include the continuity equation and momentum equations (Lesser et al., 2004; Deltares, 2013).

Continuity equation

$$\frac{\partial \zeta}{\partial t} + \frac{\partial [(d+\zeta)U]}{\partial x} + \frac{\partial [(d+\zeta)V]}{\partial y} - Q = 0 , \quad (1)$$

where ζ is the water level and d is the water depth; U and V denote the depth averaged velocities in x and y direction, respectively; and Q represents the contributions from source or sink of water per unit area.

Momentum equations in x and y direction

$$\frac{\partial u}{\partial t}+\left(u\frac{\partial u}{\partial x}+v\frac{\partial u}{\partial y}\right)-fv+g\frac{\partial \zeta}{\partial x}+\frac{C_d}{d+\zeta}u\sqrt{u^2+v^2}-\nu_H\left(\frac{\partial^2 u}{\partial x^2}+\frac{\partial^2 u}{\partial y^2}\right)=0 \quad (2)$$

$$\frac{\partial v}{\partial t}+\left(u\frac{\partial v}{\partial x}+v\frac{\partial v}{\partial y}\right)+fu+g\frac{\partial \zeta}{\partial y}+\frac{C_d}{d+\zeta}v\sqrt{u^2+v^2}-\nu_H\left(\frac{\partial^2 v}{\partial x^2}+\frac{\partial^2 v}{\partial y^2}\right)=0 \quad (3)$$

ACC HADV COR PRE BSTR VISC

where u and v denote the velocity components in x and y direction, respectively; $f=2\Omega sin\Phi$ is the Coriolis parameter depended on the geographic latitude Φ and the angular speed of rotation of the earth Ω; g is the gravitational acceleration, C_d is the bottom friction coefficient and υ_H represents the horizontal eddy viscosity coefficient. In Eq. (2) and (3), the first term stands for the local acceleration of current velocity (ACC), the second and third terms represent the horizontal advection (HADV), the fourth, fifth, sixth and seventh terms denote the Coriolis force (COR), pressure gradient (PRE) and bottom stress (BSTR), horizontal eddy viscosity (VISC), respectively. In the hydrodynamic equations Eq. (1)-(3), the principal nonlinear effects is resulted from the nonlinear free surface terms in the continuity equation (the second and third terms), and nonlinear advection (HADV) and bottom friction (BSTR) in momentum equations.

2.2 Model setup

Given that the vertical difference of current velocity is small in the situation of shallow water and tidal forcing only, an efficient two-dimensional horizontal (2DH) model is adopted in this study and focused on the horizontal patterns of tidal regimes. Moreover, relevant studies have shown that a properly configured 2DH model is able to qualitatively and quantitatively reproduce the responses of tides to coastline changes (Jia et al., 2018; Liang et al., 2018; Pelling et al., 2013; Park et al., 2014). The tidal model runs in a barotropic mode that ignores the effects of temperature, salinity and stratification as the local water column is vertically well mixed during the period of interest (Huang et al., 1999). To achieve modelling efficiency and accuracy at the same time, a double-nested scheme is used: the Bohai Sea regional model is discretized by a 372 × 470 rectangular grid with a uniform coarse grid of 1000 m. This Bohai Sea regional model is forced by 11 tidal constituents at tidal gauges Dalian and Yantai (two ends of red line in Fig. 1b), including four diurnal components (K_1, O_1, P_1, Q_1), four semi-diurnal components (M_2, S_2, N_2, K_2) and three quarter-diurnal shallow-water components (M_4, MS_4, MN_4). The harmonic constants are calculated from the hourly water level predictions by National Marine Data and Information Service of China, using the harmonic analysis tool T_tide (Pawlowicz et al., 2002). The Huanghua-Binzhou local model covers a domain of 77.1 km in NW-SE direction and 54.2 km in NE-SW direction and is driven by three open boundary conditions (orange lines in Fig. 1b) provided by the Bohai Sea regional model. The local model is run on a 328 × 269 orthogonal curvilinear boundary-fitted grid as fine as 90 m. The bathymetry data in year 2012 is used for all the model runs here, which is obtained by merging measured water depth with those

derived from navigational chart of China. The models are established based on the Gauss-Kruger projection coordinate system with the central meridian at 117°E.

2DH circulation model result is strongly dependent on the bottom friction coefficient C_d. In this study, the Manning formula is used to calculate the bottom friction, i.e., $C_d = g \cdot H^{1/3} \cdot n^2$, where g is the gravitational acceleration; H is the water depth and n is the Manning coefficient. Given local bottom roughness (sediment grain size) and bathymetry, the Manning coefficient is kept as constant at 0.0145 $m^{-1/3} \cdot s$, within the reasonable range of 0.011-0.016 $m^{-1/3} \cdot s$ in this region (Kuang et al., 2015; Song et al., 2017). The jetty and land reclamation are treated as "thin dam" (on grid boundary) and "dry point" (in grid point) in Delft3D, respectively, so that they are not erodible, and water, energy and particle transportation through them are not permitted during model simulation. The time step is 12 s so that the Courant number meets the limitation of stability and accuracy. The model is initialized from the rest ("cold start") with zero water level followed by a 4-day spin-up time to achieve hydrodynamic stability prior to the 30-day model run used for analysis.

2.3 Model validation

2.3.1 Tidal elevations

Harmonic analysis is applied to obtain the harmonic constants for astronomical tides M_2, S_2, K_1, O_1 and shallow-water tide M_4. The model-data comparison (Table 1) in the basin of Huanghua Harbor (location shown in Fig. 1c) indicates that the model results are in good agreement with the observation in October 2012, with absolute errors generally less than 5 cm and 10.5° in amplitude and phase, respectively. Followed the assessment method of

Foreman et al. (1993) given below, the vectorial differences *Diff* for M_2, S_2, K_1, O_1 and M_4 are 3.8, 3.1, 4.6, 6.4 and 1.9 cm, respectively.

$$Diff = \sqrt{(a_o \cos g_o - a_m \cos g_m)^2 + (a_o \sin g_o - a_m \sin g_m)^2} \quad (4)$$

where *a* and *g* are the harmonic amplitude and phase, respectively. The subscript *o* and *m* denote the observed and model results, respectively.

The discrepancy for the four astronomical tides is possibly induced by the coastal structures that influence the transport of tidal wave, but it is still believed to be reasonable. As for the shallow-water tide M_4, its accurate modelling is challenging because it is controlled by the local tidal dynamics, topography, bathymetry and coastline as discuss in Section 4.2, thus requires high-resolution bathymetric data and computational grid (Song et al., 2013; Suh et al., 2013). The relative error for shallow-water tide M_4 is larger than other constituents as indicated in Table 1, which is mainly triggered by the complex coastline and sparse bathymetric data within the harbor basin.

Table 1 Comparison of predicted tidal amplitudes and phases of M_2, S_2, K_1, O_1 and M_4 tidal constituents and the tidal gauge measurement at Huanghua Harbor in October 2012.

Tidal components	Amplitude (cm)			Phase (degree)			*Diff* (cm)
	Observed	Model	Error	Observed	Model	Error	
M_2	101.1	104.4	3.3	107.2	108.3	1.1	3.8
S_2	32.7	34.6	1.9	162.5	166.7	4.2	3.1
K_1	28.5	23.9	-4.6	142.1	142.3	0.2	4.6
O_1	26.5	21.7	-4.8	107.2	96.9	-10.3	6.4
M_4	3.8	2.5	-1.3	143.2	116.8	-26.4	1.9

2.3.2 Tidal currents

Field observation of tidal currents in Huanghua Harbor water was regularly carried out during harbor construction. As can be seen in Fig. 1d, the construction of Huanghua general harbor during year 2009-2012 brings in large-scale reclamation and extremely-long jetty, which may strongly impact local tidal regime. Hence, four times 25-hour data of station 1~8# (locations refer to Fig. 1c) are collected to evaluate the model performance during this period, which consist spring and neap tides (Table 2). As shown in Table 2, both the predicted tidal current velocity and direction agree well with the observation. Typically, the Pearson correlation coefficient for current velocity and direction are respectively r=0.70-0.93 and r=0.77-0.99, indicating a high collinearity. The percent bias (PBIAS) between the modelled tidal currents and the observations are mostly less than 15%, with a mean value of 9% for velocity and 7% for direction. From a harbor engineering point of view, the discrepancy of

tidal current within 20% is considered to be acceptable (Park et al., 2014; Van Maren et al., 2015) since the structure of engineering might not be accurately reproduced by the model.

In general, the overall performance of the present tidal model is comparable with that of previous models at Huanghua-Binzhou Harbor (Jia et al., 2018; Feng et al., 2008; Kuang et al., 2015; Song et al., 2017), and can be used with confidence for modelling of tidal dynamics in different construction phases of Huanghua-Binzhou Harbor.

Table 2 Assessment of current velocity and direction for station 1~8# (locations refer to Fig. 1c) in the vicinity of Huanghua-Binzhou Harbor during year 2010-2012

Time	Stations	Velocity ($m \cdot s^{-1}$)		Direction (degree)	
		r	*PBIAS* (%)	*r*	*PBIAS* (%)
2010.09.14-15 (Neap tide)	1#	0.71	7.7	0.90	-1.7
	2#	0.73	-3.9	0.89	8.0
	3#	0.89	8.8	0.89	9.6
	4#	0.89	-3.1	0.94	1.2
2010.09.27-28 (Spring tide)	1#	0.91	13.9	0.95	-6.7
	2#	0.70	-0.6	0.99	14.0
	3#	0.70	7.3	0.83	7.5
	4#	0.86	-7.2	0.95	14.8
2011.09.27-28 (Spring tide)	2#	0.92	-5.0	0.83	7.4
	5#	0.88	-15.6	0.84	4.6
	6#	0.80	-17.0	0.79	9.5
	7#	0.93	-4.9	0.98	4.7
	8#	0.89	-9.0	0.81	1.2
2012.10.15-16 (Neap tide)	2#	0.78	10.1	0.84	-11.8
	5#	0.77	-9.5	0.82	-4.4
	8#	0.78	-19.5	0.77	-0.6

2.4 Numerical model implementation

Based on the well-validated tidal model, ten numerical experiments (Table 3) are conducted to investigate the response of tidal dynamics to coastlines change with special attention to the physical mechanism of M_2 and M_4 tidal modification. The baseline run (Run 1) is forced with all 11 tidal components (K_1, O_1, P_1, Q_1, M_2, S_2, N_2, K_2, M_4, MS_4, MN_4), with a coastline of year 2003 before large-scale harbor constructions. To illustrate the tidal energy transport of the pronounced astronomical tides in the Bohai Sea, two additional numerical experiments are conducted only considering the tidal forcing of M_2 (Run 2) and K_1

283 (Run 3) at the open boundary, respectively. Then, the coastline of year 2003 in baseline run is
284 replaced with that in year 2006, 2012 and 2016 to analyze the changes in tidal energy flux,
285 total tidal energy density and tidal constituents M_2 and M_4. Finally, a series of sensitivity
286 studies of shallow-water tide M_4 (Run 7 to Run 10) is carried out. Run 7, Run 8 and Run 9
287 exclude the fundamental tide M_2, shallow-water tides (M_4, MS_4 and MN_4) and other
288 semidiurnal tides (S_2, N_2, and K_2), respectively, to assess the energy transfer from M_2 to M_4.
289 Run 10 changes the bathymetry shallower than 4 m to uniform 4 m for evaluating the role of
290 bottom slope in energy transfer.
291
292 **Table 3** Summary of numerical model experiments

No.	Tidal forcing	Coastline	Remark
Run1	K_1, O_1, P_1, Q_1, M_2, S_2, N_2, K_2, M_4, MS_4, and MN_4	2003	Baseline run
Run2	Only M_2	2003	
Run3	Only K_1	2003	
Run4	Same as Run 1	2006	
Run5	Same as Run 1	2012	
Run6	Same as Run 1	2016	
Run7	Same as Run 1 but excludes M_2	2003	
Run8	Same as Run 1 but excludes M_4, MS_4 and MN_4	2003	
Run9	Same as Run 1 but excludes S_2, N_2, and K_2	2003	
Run10	Same as Run 1	2003	Change variable water depth shallower than 4 m to constant 4 m water depth

293
294

2.5 Tidal energy propagation speed

2.5.1 Tidal energy

The tidal energy flux over a unit width within one tidal circle $\vec{E}_f$ and the total tidal energy (including potential and kinetic tidal energy) per unit area E, i.e. total tidal energy density, can be determined by the following two equations, respectively (Song et al., 2013; Guo et al., 2018):

$$\vec{E}_f = \frac{1}{T}\int_0^T \rho D\left(g\zeta + \frac{1}{2}|\vec{v}|^2\right)\vec{v}\,dt \tag{5}$$

$$E = \frac{1}{2}\rho\left(g\zeta^2 + D|\vec{v}|^2\right) \tag{6}$$

where T is the tidal period, ρ is the water density, $D=H+\zeta$,ζ is the water level and H is the mean water depth, and $\vec{v}$ is the velocity vector.

2.5.2 Tidal wave propagation speed

The propagation speed of tidal wave, C, can be calculated from the co-phase chart of the tidal constituent (Wu et al., 2018):

$$C=L\cdot T^{-1} \tag{7}$$

where L, $T=(\Delta g/360°)\times T_0$ and Δg are the distance, travel time, the phase between two adjacent co-phase lines, respectively, and T_0 is the period of tide.

3 Model Results

3.1 Tidal dynamics in the Bohai Sea

Located in a semi-closed domain, tidal dynamics in the Bohai Sea is strongly influenced by the tidal waves traveled from north of the Yellow Sea. As suggested in previous studies, semi-diurnal M_2 tide contributes the most to the regional tidal energy, followed by diurnal K_1 tide (Bao et al., 2001; Song et al., 2013). The averaged tidal energy flux of M_2 (Run 2) and K_1 (Run 3) tides are shown in Fig. 2a and 2b, respectively. It is evident that after entering the Bohai Sea, the M_2 tidal energy flux breaks into two main branches over the Bohai Strait, one branch travels towards the Liaodong Bay and the other travels westerly into the Bohai Bay. Both branches of M_2 tidal energy flux experience counter-clockwise rotation due to the Coriolis force, thus form amphidromic points at the Qinhuangdao coast and the entrance of Yellow River accordingly (Fig. 2c), due to the tidal energy reflection by the coast (Bao et al., 2001). The K_1 tide enters the Bohai sea at the north of the Bohai Strait then counter-clockwisely travels along the coast with an energy flux magnitude of 10^3- 10^4 $W \cdot m^{-1}$, and eventually exits the Bohai sea at the south of the Bohai Strait. As a result, an amphidromic point of K_1 tide is formed in the middle of the Bohai Strait (Fig. 2d). The semi-diurnal S_2 and diurnal O_1 tides have similar spatial variation as the M_2 and K_1 tides, respectively, but with smaller magnitudes (not shown). Our model results of tidal dynamics are generally consistent with the previous tidal model studies of the Bohai Sea (e.g. Fang et al., 2004; Pelling et al., 2013; Song et al., 2013; Xie et al., 1990; Zhu et al., 2018).

335

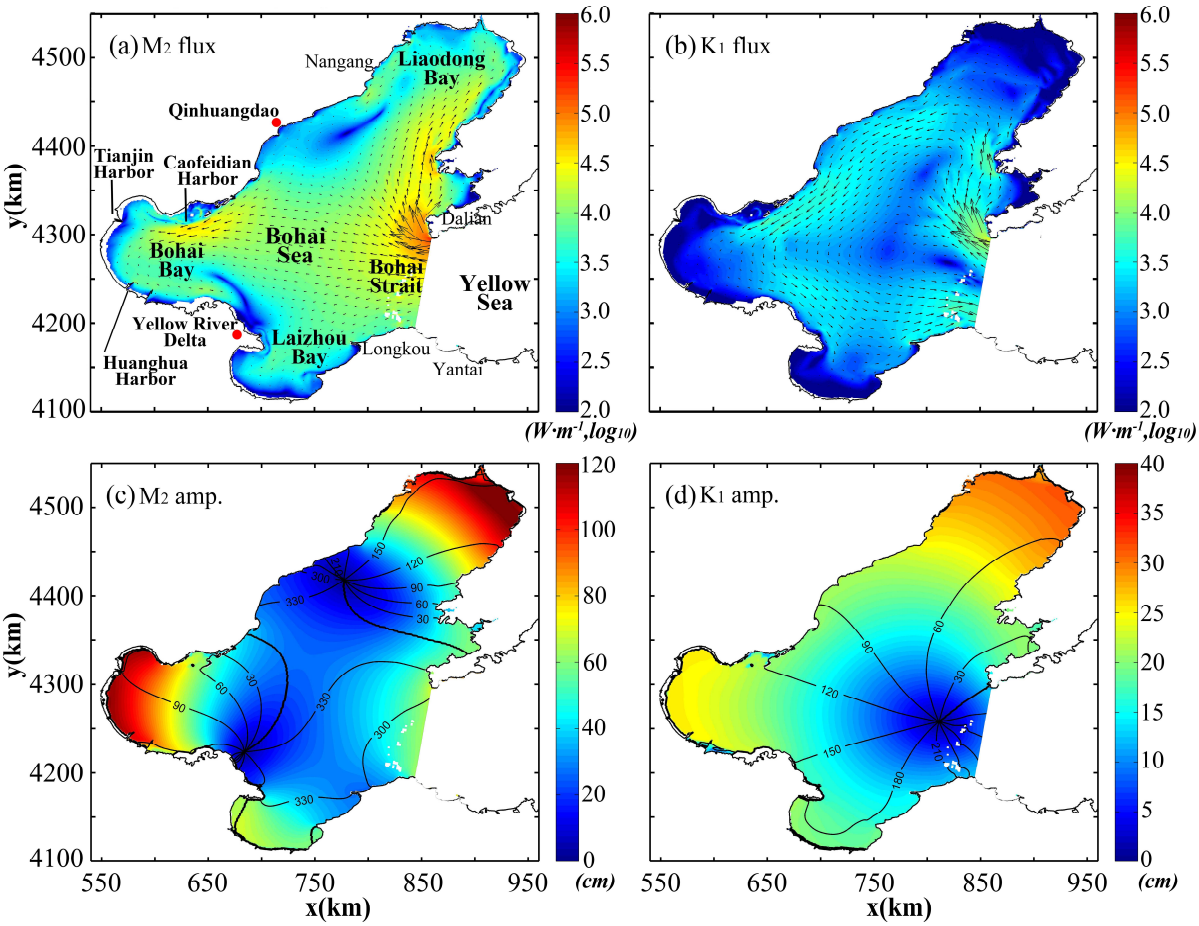

336

337 Fig. 2. Averaged tidal energy flux of (a) semidiurnal tide M_2 and (b) diurnal tide K_1 in the

338 Bohai Sea. Vectors represents the direction of energy flux and color contour map indicates

339 the log-10 magnitude of energy flux, unit: $W \cdot m^{-1}$. Tidal amplitude (contour map, unit: cm)

340 and co-phases lines (contour lines, unit: degree) of (c) M_2 and (d) K_1 tides in the Bohai Sea.

341

342

343 **3.2 Tidal dynamics in Huanghua-Binzhou Harbor in year 2003**

344 The Huanghua-Binzhou Harbor lies in southwestern Bohai Bay and is controlled by the
345 west branch of M_2 tidal wave. According to the harmonic analysis in Section 2.3.1, local tidal
346 amplitudes of M_2 is at least three time larger than that of diurnal tides K_1 and O_1 and
347 semi-diurnal tide S_2 (Table 1). Therefore, the following sections will focus on the dominant
348 M_2 tide, and its first overtide M_4, which tends to be the most energetic shallow-water tide
349 (Aubrey and Speer, 1985; Speer and Aubrey, 1985).

350 ***3.2.1 Tidal constituents M_2 and M_4***

351 The Bohai Bay is a typical C-shaped shallow-water bay with a mean water depth of 13
352 m, and a depth of 20 m in the centre of the bay. While M_2 tidal wave travels
353 counter-clockwisely over the bay, the maximum tidal amplitude occurs at the head of the bay
354 as shown in Fig. 2c, due to shoaling (Song et al., 2013; Li et al., 2018a), geometrical
355 convergence (Dyer, 1973) and wave reflection (Bao et al., 2001). Then, the M_2 tidal wave
356 travels southeasterly through the Huanghua-Binzhou Harbor with a faster tidal wave speed of
357 30 $m \cdot s^{-1}$ in the coast and a slower speed of 16 $m \cdot s^{-1}$ in the offshore area (wave speed is
358 calculated from the co-phase lines in Fig. 3a according to Eq. (7)). Correspondingly, the M_2
359 tidal amplitude decreases from 120 cm in the west of Huanghua Harbor to 85 cm in the
360 northeastern deeper waters as shown in the contour map in Fig. 3a.

361 The nonlinearity of the tide is enhanced by the relative shallow water depth, and
362 produces intensive M_4 tide in coastal area. As shown in Fig. 3b, M_4 tidal amplitude increases
363 towards the shoreline markedly from 4 cm to 16 cm on the tidal flat, especially in the area

shallower than 4 meter (the red line in Fig. 3b). It is worth noticing that spatial distribution of M_4 amplitude appears to have a wider range with larger magnitude (reaching 20 cm) in the vicinity of Binzhou Harbor, which is considered to be relative with the gentler slope and stronger nonlinearity there (see further discussion in section 4.2.1). The modelling of shallow-water tides in the Bohai Bay is rare and our modelled result of M_4 tide is basically consistent with that reproduced by Xie et al. (1990) and He et al. (2004). As can be seen in Fig. 3b, there is an amphidromic point of M_4 tide existing near the centre of Bohai Bay where local nonlinear dynamics is weaker than the coast ones; and M_4 tide also experiences a counter-clockwise rotation, the same as the M_2 tidal wave.

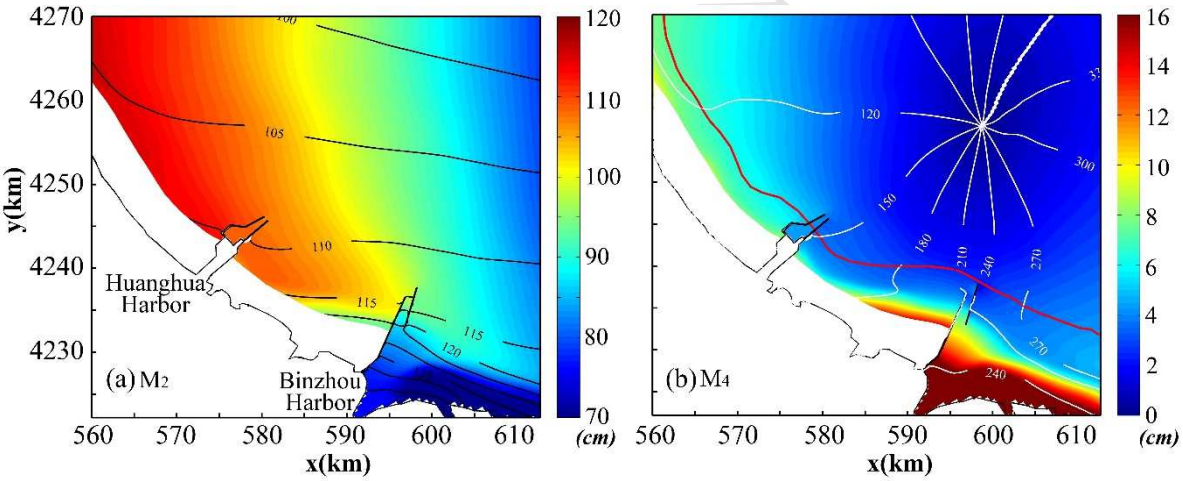

Fig. 3. Tidal amplitude (contour map, unit: cm) and co-phases lines (contour lines, unit: degree) of (a) semidiurnal tide M_2 and (b) its overtide M_4 tide in the Huanghua-Binzhou Harbor and adjacent coast. Red line in (b) represents the isobath of 4 m.

3.2.2 Tidal energy flux and density

Under the influence of the M_2 tidal wave described above, the Huanghua-Binzhou coast is dominated by a flood tide and a counter-clockwisely rotating tidal current (Kuang et al., 2015). The phase difference between tidal elevation and tidal current is nearly 90°, indicating

a standing wave in this region. As demonstrated in Fig. 4a, in the offshore area, the tidal energy flux is in the onshore direction with a magnitude of about 3.0×10^4 W·m^{-1}. However, in coastal area, the tidal energy flux is deflected to southeasterly alongshore transport due to the diversion by the coastline, in particular around the head of the jetties at Huanghua and Binzhou harbors. The spatial variation of tidal energy flux (contour map in Fig. 4a) generally follows the pattern of the bathymetry as the deeper water has larger water depth and higher velocity. In comparison, the tidal energy flux in this region is about two order of magnitude smaller than those in Yellow Sea and East China Sea (Song et al., 2013; Suh et al., 2014; Guo et al., 2018). This is because only a small portion of the pronounced M_2 tidal energy in Yellow Sea enters into the Bohai Sea (Song et al., 2013; Suh et al., 2014), resulting in a weaker tidal dynamics in this region and that tidal energy dissipation is enhanced at the shallower water depth in this region (Li et al., 2018a).

The tidal energy density is composed of potential tidal energy density (PTE) and kinetic tidal energy density (KTE) as indicated in Eq. (6). In general, the averaged energy density (Fig. 4b) is dominated by PTE that decreases southeasterly from 5.5 KJ·m^{-2} to 3.0 KJ·m^{-2} (Fig. 4c). It is not surprise to see that the spatial distribution of PTE (a function of water level ζ) has a similar pattern to M_2 tidal amplitude (Fig. 3a) which is the key contributor to the local water level ζ, therefore, PTE. In contrast, KTE decreases from 2.0 KJ·m^{-2} in the offshore area to less than 0.2 KJ·m^{-2} towards the shore (Fig. 4d), due to decreasing water depth and weakened current velocity by the onshore increased dissipation. As a result, the ratio of KTE to the total tidal energy density attains its maximum of ~45% in the offshore and decays rapidly towards the coast.

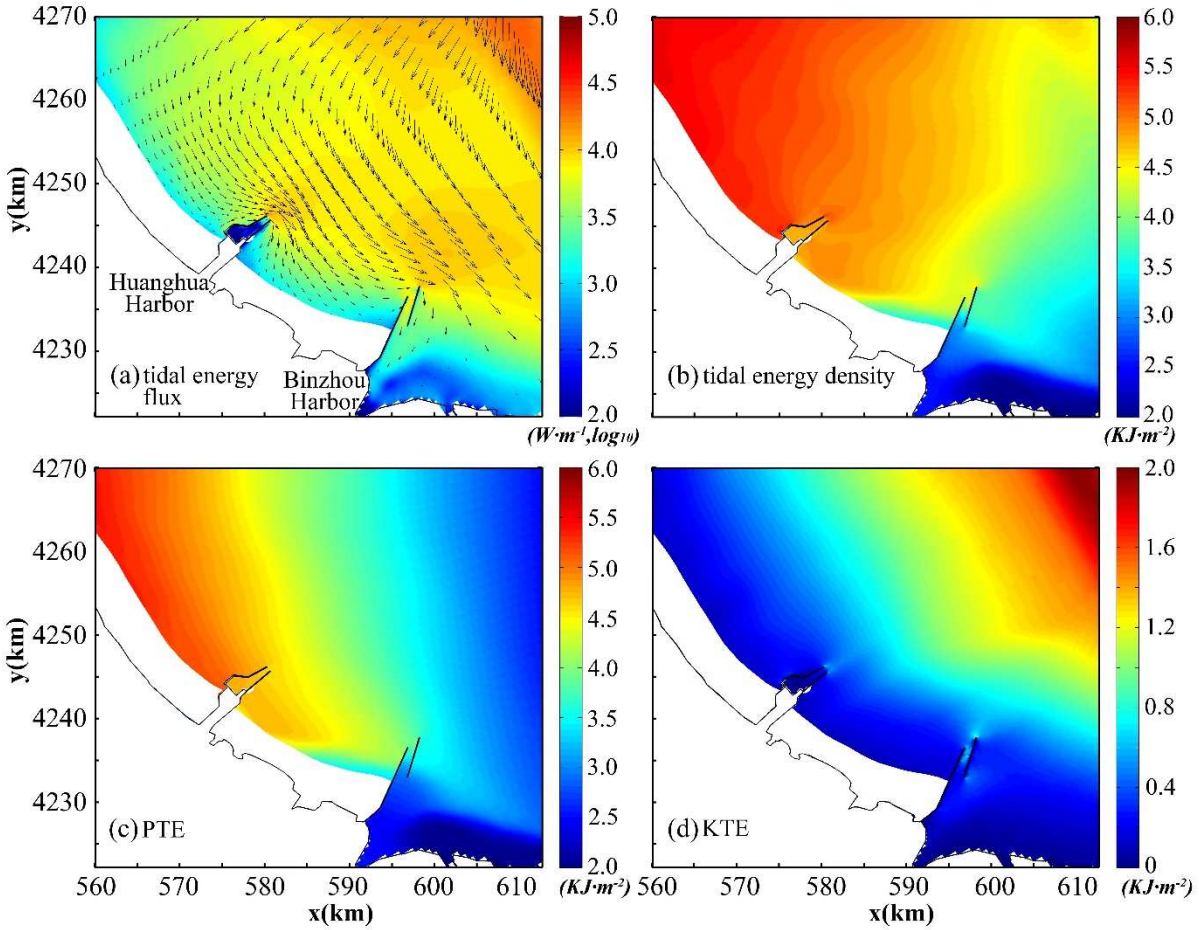

Fig. 4. (a) Averaged tidal energy flux. Vectors represents the direction of energy flux and color contour map indicates the log-10 magnitude of energy flux, unit: $W \cdot m^{-1}$. Averaged (b) total tidal energy density (unit: $KJ \cdot m^{-2}$), (c) potential tidal energy density (unit: $KJ \cdot m^{-2}$) and (d) kinetic tidal energy density (unit: $KJ \cdot m^{-2}$).

3.3 Tidal responses to harbor constructions during year 2006-2016

3.3.1 Tidal constituents

During the harbor constructions in year 2006-2016 (Fig. 5a-c), the predominant M_2 tidal wave is supposed to be reflected by the coastal structure that is treated as wall boundary condition (Song et al., 2013). As can be seen, M_2 tidal amplitude increases on the stoss side and decreases on the lee side of the jetties correspondingly, by about 2 cm, in 2006 (Fig. 5a).

The sequential harbor constructions in 2012 and 2016 result in similar variation pattern of M_2 tidal amplitude, but with larger magnitude of 3 cm in 2012 and 6 cm in 2016 (Fig. 5b and 5c). This striking variation pattern of M_2 tidal amplitude, i.e. increases (decreases) on the stoss (lee) side, is also noticed in other regions, e.g., the Yangshan Harbor (Guo et al., 2018) and Taiwan Strait (Dai et al., 2017). Fig. 5 also shows that the tidal amplitude change mainly occurs around Hunaghua Harbor, and the impact of Binzhou Harbor is not as pronounced due to the sheltering effect of Huanghua Harbor.

The spatial distributions of amplitude change of nonlinear shallow-water tide M_4 (Fig. 5d-f) is highly correlative with those of M_2 tide (Fig. 5a-c) since M_2 is the energy source of M_4 (Parker, 1991; Blanton et al, 2002). But there are some discrepancies between the variation pattern of M_2 and M_4 tides (marked as the red boxes in Fig. 5d), which are likely induced by the changes of local dominating nonlinear term (further discuss in Section 4.2.2). In comparison, the shallow-water tide M_4 responds more strongly to the bathymetric and coastline geometrical changes (Gao et al., 2014) than the predominant M_2 tide in this region, with a much larger change rate in tidal amplitude (~25% vs. ~5%). The large-scale construction of Binzhou Harbor in 2016 has more profound influence on M_4 tide than that of Huanghua Harbor, causing M_4 amphidromic point to retreat significantly towards the coast (contour lines in Fig. 5f). The magnitude of M_4 tidal modification seems to be related to the location of the construction (cf. Gao et al., 2014; Liang et al., 2018) as the Binzhou Harbor is constructed on the shallower southeastern region with relatively large M_4 amplitude (see Fig. 3b).

436

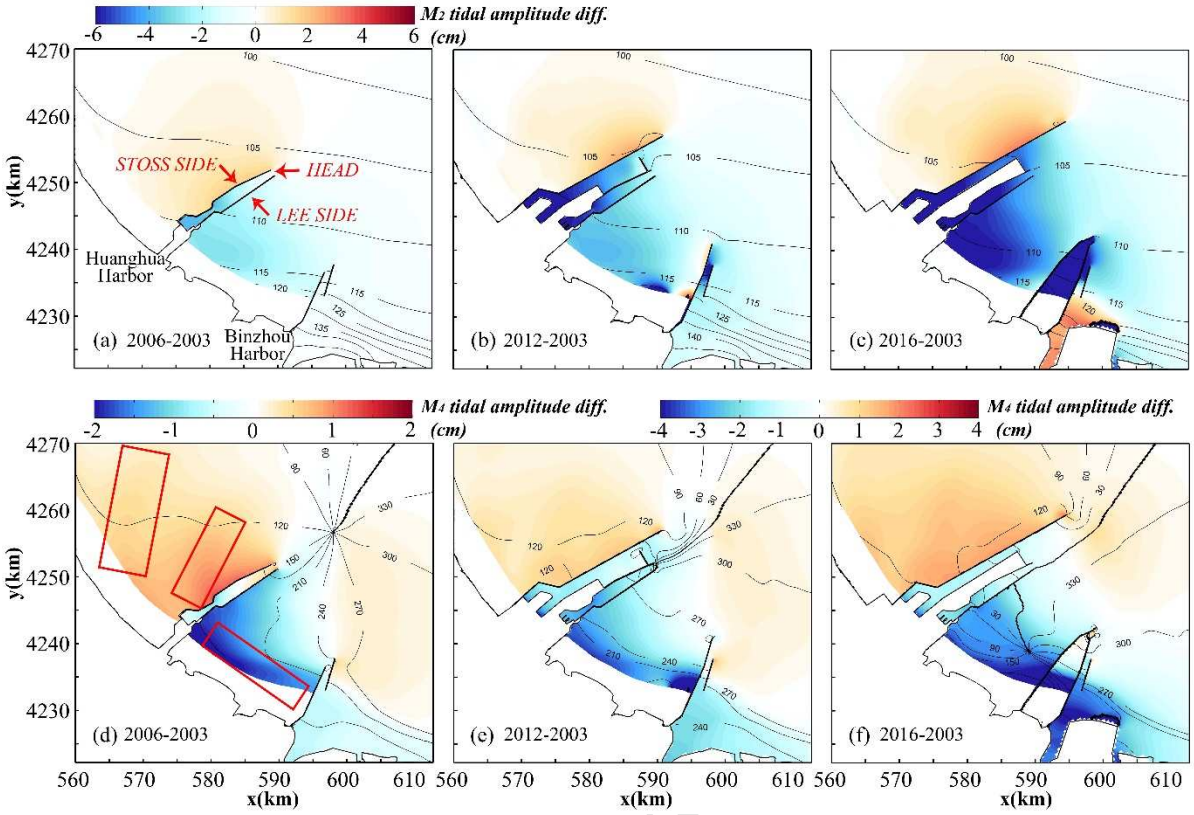

437

438 Fig. 5. Changes of M_2 and M_4 tidal amplitude (unit: cm) (a) & (d) between year 2006 and
439 2003; (b) & (e) between year 2012 and 2003; (c) & (f) between year 2016 and 2003 due to
440 the three phases of harbor construction in these time periods. Contour lines indicate the
441 co-phase lines (unit: degree) in corresponding construction phase.

442 ***3.3.2 Tidal energy***

443 As harbor jetties are often constructed along the direction of local tidal current, the
444 dominant SW-NE (cross-shore) tidal current in the Huanghua-Binzhou Harbor thus has less
445 change by the jetties, while the alongshore one decreases around the middle of jetty and
446 increases at the head of jetty (Song et al., 2017). Furthermore, tidal current velocity modifies
447 tidal energy flux more than water level , not only because tidal energy flux is a cubic function
448 of the former and linear function of the latter (cf. Eq. (5)), but also the variation of the former

449 is one order of magnitude larger than that of the latter. As a result, the transport of tidal
450 energy is subject to more profound influence in alongshore direction than cross-shore
451 direction (Fig. 6a-c). It shows that the tidal energy propagation from northwest to southeast is
452 obstructed severely by both sides of the harbors but enhanced at the jetty head, leading to
453 striking "butterfly-shaped" variation patterns. The area over which the tidal energy flux is
454 modified by the harbor constructions on the stoss side is larger than that on lee side of the
455 harbors, with a magnitude of 0.8-5.5 KW·m^{-1}.

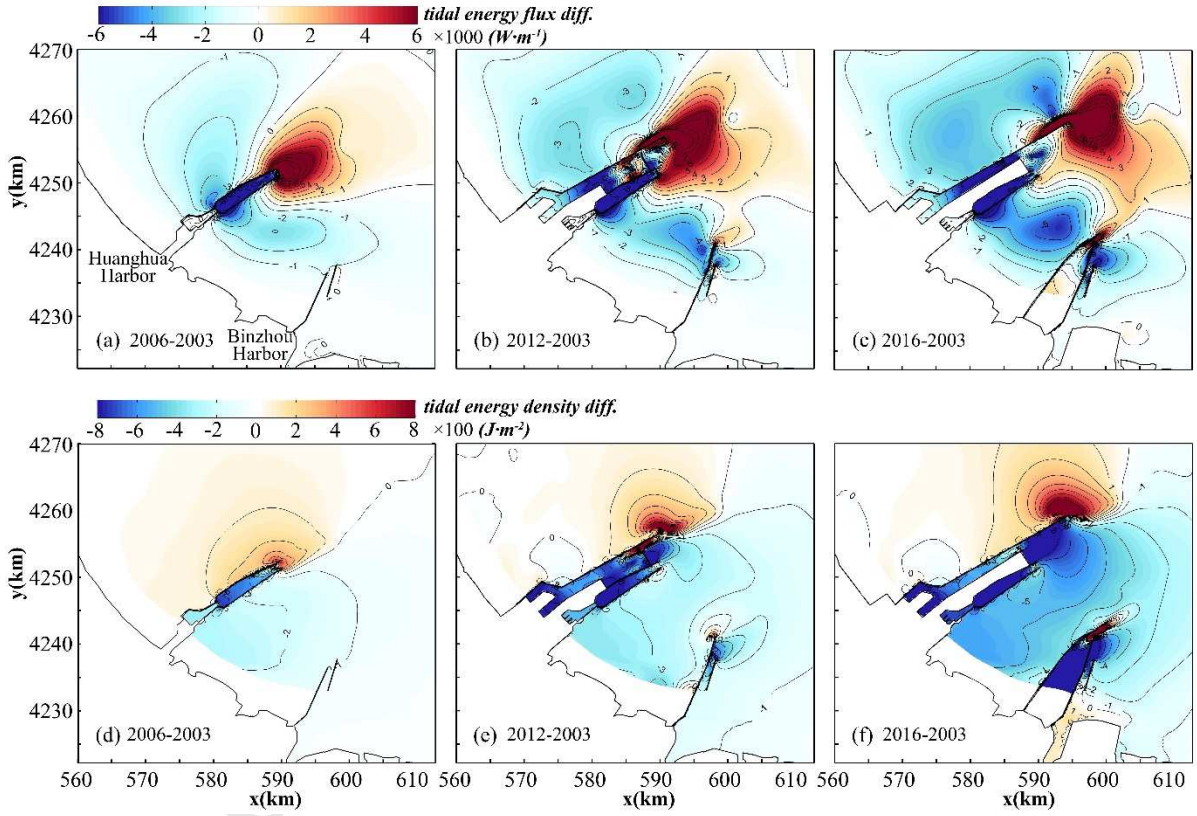

456

457 Fig. 6. Changes of tidal energy flux (unit: W·m^{-1}) and tidal energy density (unit: J m^{-2}) (a) &
458 (d) between year 2006 and 2003; (b) & (e) between year 2012 and 2003; (c) & (f) between
459 year 2016 and 2003 due to the three phases of harbor construction in these time periods.

460 The total energy density in coastal region is therefore to be redistributed due to the
461 change of tidal energy transport. Different from the harbor constructions in deep waters (Guo

et al., 2018), the coastal structures in Huanghua-Binzhou coast led to much more complex change of tidal energy density (Fig. 6d-f): as the harbor extends further offshore sequentially, the total tidal energy density is increased by 0.2-0.6 KJ·m^{-2} on the stoss side of Huanghua Harbor but is decreased on the lee side accordingly. Moreover, the changes in the total tidal energy is primarily attributed to the potential tidal energy (PTE) (Fig. 7a-c), while the kinetic tidal energy (KTE) only contributes to the changes at the head of jetties (Fig. 7d-f).

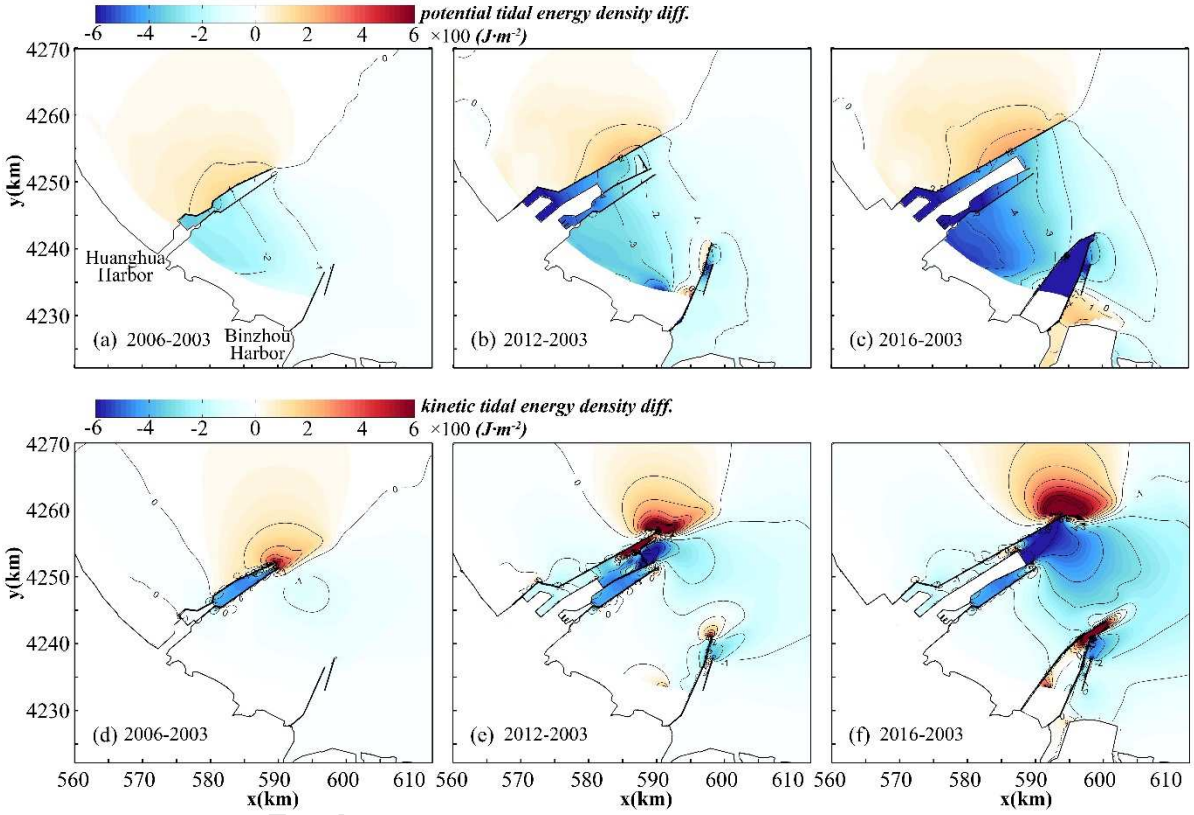

Fig. 7. Changes of potential and kinetic tidal energy density (unit: J·m^{-2}) (a) & (c) between year 2006 and 2003; (b) & (e) between year 2012 and 2003; (c) & (f) between year 2016 and 2003 due to the three phases of harbor construction in these time periods.

Finally, the southeasterly decreasing pattern of total tidal energy density in 2003 (Fig. 4b) is then divided into two branches by the jetty built in 2006: the one on the stoss side becomes more energetic while the one on the lee side becomes less energetic (Fig. 8a). This

phenomena is further strengthened by the further construction of Huanghua Harbor in the second phase in 2012 (Fig. 8b). When the extremely long jetty of Huanghua Harbor completed in 2016, there is a significant reduction in tidal energy in the region between two harbors, resulting in three prominent separated bands of tidal energy density in this region, with values of 5.5 KJ·m^{-2}, 4.3 KJ·m^{-2} and 3.2 KJ·m^{-2}, respectively (Fig. 8c).

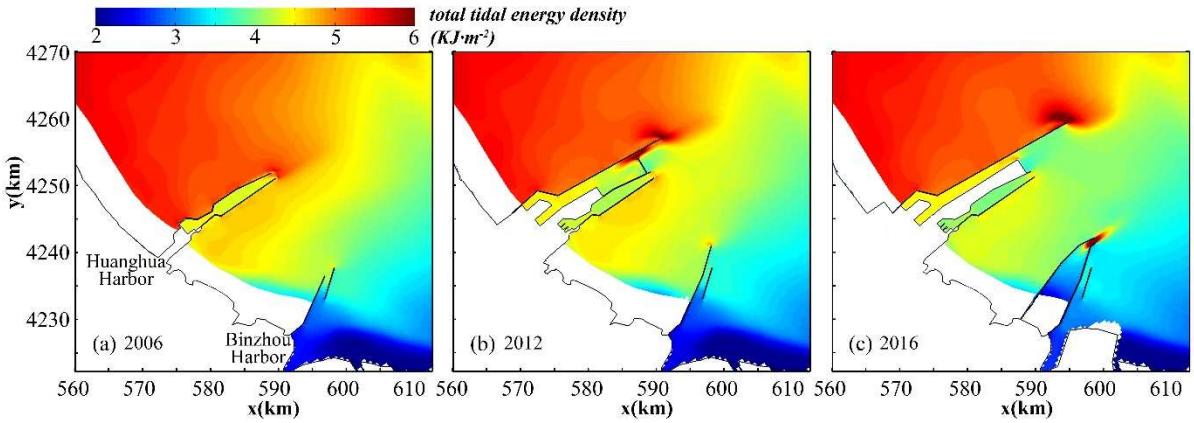

Fig. 8. Total tidal energy density at the three phases of Huanghua-Binzhou Harbor construction (a) 2006, (b) 2012 and (c) 2016 (unit: KJ·m^{-2}).

In fact, reclamation can release the tidal energy stored and dissipated over the reclaimed area (Song et al., 2013). However, the released tidal energy by the harbor constructions here takes up only a small portion of the changed total tidal energy, around 10%. Thus, the tidal energy redistribution is mainly induced by the long jetties that modify the way of tidal energy propagation along the Huanghua-Binzhou coast. Obviously, the obstruction effect of jetty causes more tidal energy to be stored on the stoss of Huanghua Harbor (Fig. 6d-f), most of which is converted to PTE and some to the KTE (Fig. 7). The opposite trend in changes is then achieved on the lee side. Therefore, it is not surprise to find that the variation pattern of M_2 tidal amplitude changes (Fig. 5a-c) is largely consistent with that of PTE (Fig. 7a-c) as the

493 M_2 tide plays a major role in the local tidal elevation (i.e. potential tidal energy). Moreover,
494 M_2 tide is respond more to the coastline and geometric changes due to the constructions of
495 two harbors and their extensions than the diurnal tidal wave (K_1 and O_1). It is because the
496 latter has longer wave length, therefore, suffers less effect from the obstacle of structures (Wu
497 et al., 2018).
498

4 Discussion

4.1 Momentum balance

Following Hench and Luettich (2003), the tidal dynamics is analyzed in this section by comparisons of the model results of momentum terms. The model results at maximum flood, mid flood (1.5 hours after maximum flood) and high tide in year 2006 are taken as an example to evaluate the momentum balance in the vicinity of Huanghua jetties. Then, the relationship between momentum change and tidal distortion is discussed. In this study, the momentum change due to turbulent viscosity (VISC) is not discussed for it is at least one order smaller than other terms.

4.1.1 Spatial distribution of momentum terms

At maximum flood, the current field has reached quasi-static state (Fig. 9a), therefore, weak acceleration (ACC) (Fig. 10a1 and 10b1) compared with other tidal phases. The pressure gradient (PRE) plays a crucial role in the momentum balance at this tidal phase, with a magnitude of up to 8.2×10^{-5} m•s^{-2} (Fig. 10c1 and 10d1). Meanwhile, the large cross-shore current results in large Coriolis force (COR) in alongshore, *m* direction (Fig. 10e1), and bottom friction (BSTR) in cross-shore, *n* direction (Fig. 10h1), with a magnitude of 4-6 $\times$ 10^{-5} m•s^{-2}. These two terms play a secondary role in the momentum balance to balance the PRE terms in *m* and *n* directions, respectively. The horizontal advection (HADV) becomes important at the head of jetties where current changes greatly and strong nonlinearity occurs (Fig. 10i1 and 10j1).

520 At mid flood, momentum balance is mainly between local acceleration and pressure
521 gradient. It shows that the tidal flood flow (Fig. 9b) is accelerated towards the southeast (Fig.
522 10a2) by the favorable pressure gradient in the alongshore direction, as shown in Fig. 10c2
523 (the negative PRE indicates a southeasterly downward slope of water surface). However, the
524 onshore tidal current is decelerated markedly (Fig. 10b2) by the adverse pressure gradient in
525 cross-shore direction, as shown in Fig. 10d2 (the positive PRE indicates an onshore upward
526 slope of water surface), which is formed by the piled-up water against the coast during flood.
527 In comparison, the momentum balance is contributed less by COR, BSTR and HADV (Fig.
528 10e2-j2), due to smaller current at mid flood.

529 At high tide, the tidal current is weak and complex (Fig. 9c) and the difference of water
530 level between two sides of the harbor reaches the maximum (see Fig. 9f). The waters on the
531 stoss side of jetties is supposed to move to the other side for compensating the imbalance of
532 pressure gradient between two sides. Thus the positive pressure gradient in the cross-shore
533 direction (Fig. 10d3) plays an opposite role to the current flow on the stoss side, i.e. it shifts
534 to accelerate the offshore flow as the flow direction (Fig. 9c) is in accordance with
535 acceleration direction (Fig. 10b3) (note that the acceleration direction is opposite to positive *n*
536 direction so that a negative value in local ACC). Consequently, the flow on stoss side is
537 driven by the pressure gradient to transport offshore and converges at the head of jetties,
538 resulting in a pronounced offshore acceleration (Fig. 10b3). Around the head of jetties, the
539 current is strongly accelerated to the southeast under the favorable influence of PRE in
540 alongshore direction (Fig. 10c3) and finally enters the lee side of Huanghua jetties. The
541 contribution from COR and BSTR is even smaller at this tidal phase (Fig. 10e3-h3) compared

542 to those at flood, but the HADV contributes a lot to the momentum balance at the head of
543 jetties (Fig. 10i3 and 10j3) and is primarily balanced by PRE. This is because while the tide
544 rotates clockwisely around the head of jetties, tidal current reaches 1 $m \cdot s^{-1}$ accompanied by a
545 significant change in direction (Fig. 9c), and therefore causes strong horizontal advection.

546 In summary, pressure gradient plays a dominant role in the momentum balance in the
547 vicinity of Huanghua jetties in 2006, with a strength of up to nearly 1.0×10^{-4} $m \cdot s^{-2}$. In the
548 deeper waters, the PRE is primarily balanced by ACC and COR but little impact arising from
549 the nonlinear terms, following linear wave dynamics (Hench and Luettich, 2003; Guo et al.,
550 2018). As water depth decreases, the contribution from BSTR gradually increases due to the
551 enhanced bottom friction. Hence, the momentum balance in shallow water is dominated by
552 BSTR and PRE (Speer and Aubrey, 1985). The horizontal advection (HADV), which is not
553 as importance in most of our study region, attains its maximum values at the head of jetties at
554 high tide when current is characterized by great changes in spatial gradient. Strong HADV
555 has been linked to the rapid changes of coastline, topography and bathymetry (Speer and
556 Aubrey, 1985). Moreover, the fact that the intense horizontal advection is mainly balanced by
557 the pressure gradient suggests a quasi-Bernoulli flow (Guo et al., 2018; Wu et al., 2018).
558

559

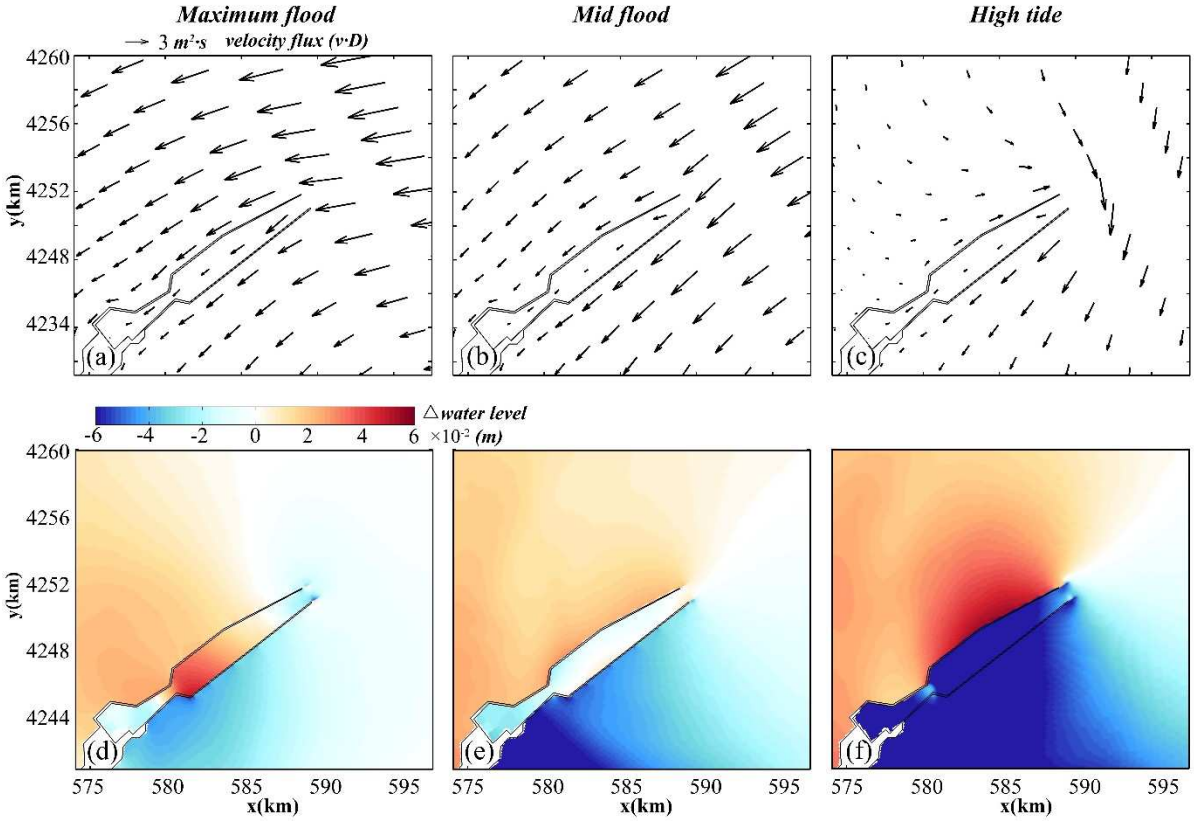

560

561 Fig. 9. (Upper) Velocity fluxes (i.e., current velocity *v* times water depth *D*) in the

562 construction phase of 2006 and (Lower) change in water level (year 2006-2003) around

563 Huanghua jetties at (a)&(d) maximum flood, (b) & (e) mid flood and (c) &(f) high tide.

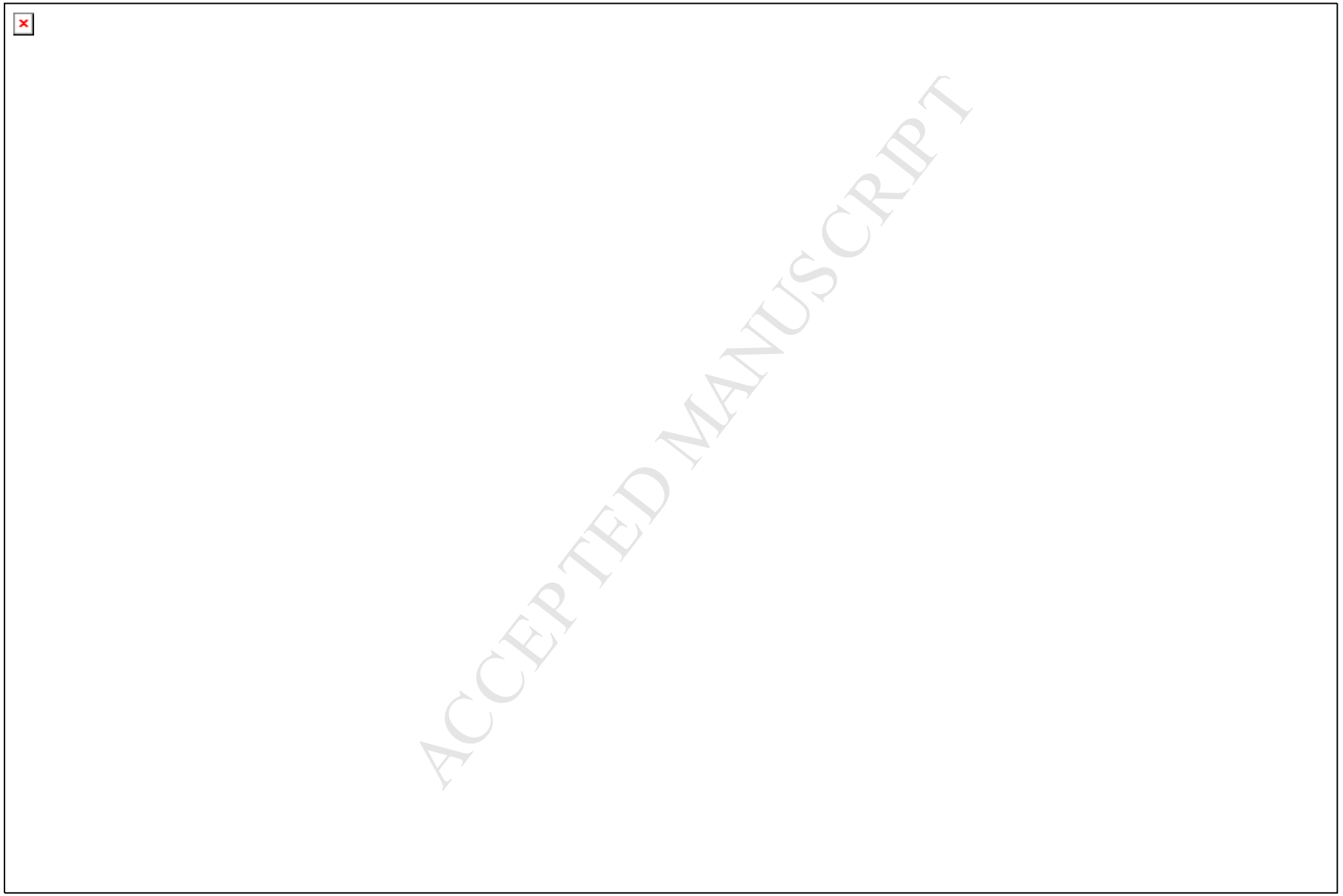

564

Fig. 10. Momentum balance terms around Huanghua jetties at (a1)-(j1) maximum flood, (a2)-(j2) mid flood and (a3)-(j3) high tide in year 2006. First Row: ACC (acceleration of tidal current); Second Row: PRE (pressure gradient); Third Row: COR (Coriolis force); Fourth Row: BSTR (bottom friction); Fifth Row: HADV (horizontal advection). Left Column: alongshore, *m* direction; Right Column: cross-shore, *n* direction. Red dots in (j3) denote the locations of station S and station L used for analyzing momentum changes in Section 4.1.2.

569 ***4.1.2 Momentum change in tides***

570 To gain further insight into the mechanisms of M_2 amplitude change (Fig. 5a-c), the
571 jetty-induced changes (year 2006-2003) of momentum terms and water levels at Station S
572 and L (location refer to Fig. 10j3) during one tidal cycle are demonstrated in Fig. 11. Because
573 of the dominance of ACC-PRE momentum balance around Huanghua jetties, these two
574 momentum terms appear to experience the largest changes due to constructions, which can
575 reach 1.2×10^{-4} m·s^{-2}. In addition, ACC and PRE balance each other within one tidal cycle
576 (Fig. 11), suggesting the energy transfer between potential energy and kinetic energy. In
577 comparison, the changes of HADV, COR and BOT are comparable to ACC and PRE but not
578 more than 5.0×10^{-5} m·s^{-2}.

579 The results on the stoss side of jetty are demonstrated in Fig. 11a-c. As shown, the jetties
580 block the velocity component in the alongshore direction and lead to a decreased ACC in
581 alongshore, *m* direction, during flood (Fig. 11b), and the maximum decrease in ACC occurs
582 at high tide. The maximum increase of pressure gradient is thus correspondingly obtained at
583 high tide due to the piled-up water, with a more southeasterly upward slope of water surface
584 compared with that in 2003 (Fig. 9f). On the contrary, the maximum decrease of PRE (a more
585 downward slope southeastward) is achieved just after low tide (Fig. 11b). Similar variation
586 patterns happen to the momentum changes in cross-shore, *n* direction (Fig. 11c). On the other
587 side of harbor, the lee side, momentum changes between ACC and PRE in cross-shore
588 direction (Fig. 11f) is more predominant than those in alongshore direction (Fig. 11e),
589 especially just after high tide and low tide. This can be explained by the fact that cross-shore
590 current on the lee side is greatly directed by the newly-built jetties during these tidal phases

(e.g. Fig. 9c), therefore resulting in larger momentum changes in cross-shore direction. On the contrary to that of stoss side (Fig. 11b), the maximum increase/decrease of PRE on the lee side is achieved at low/high tide (Fig. 11f).

In Section 3.3, we have shown the harbor constructions can bring in potential tidal energy, also M_2 tidal amplitude, increased on the stoss side and decreased on the lee side (Fig. 5a-c and Fig. 7a-c). In response to this tidal distortion, water level in 2006 appears to have higher high tide and lower low tide (i.e. a larger tidal range) on the stoss side compared to that in 2003 (Fig. 11a); whereas, lower high tide and higher low tide (i.e. a smaller tidal range) on the lee side (Fig. 11d). Comparing the variation patterns of water level and pressure gradient, it is noted that the significant changes of water level on the stoss side and lee side are more consistent with the corresponding changes of pressure gradient in alongshore direction and cross-shore direction, respectively (cf. black dashed line in Fig. 11a with black solid in Fig. 11b and black dashed line in Fig. 11d with black solid line in Fig. 11f). This qualitative analysis indicates that the jetties have greater impacts on the stoss side alongshore current and the lee side cross-shore current, which results in a larger tidal range on the stoss and a smaller tidal range on lee side, respectively. This finding is likely to be applicable to the similar variation pattern of M_2 amplitude in the Yangshan Harbor (Guo et al., 2018) and Taiwan Strait (Dai et al., 2017), where local structures block the traveling M_2 tide and leads to an increase on the stoss side and a decrease on the lee side. However, the construction of Saemangeum Dyke leads to an overall decrease of M_2 amplitude in the local (Lee et al., 2008; Suh et al., 2014; Park et al., 2014). Specifically, on its southern side, i.e., the stoss side of M_2 tidal wave propagating, the decrease of local M_2 amplitude is also considered to be relative

613 with the modified pressure gradient due to the change of flow (Park et al., 2014). This
614 opposite response of M_2 tide to the present study is unclear but could be explained from
615 energy point of view as: the Saemangeum Dyke is roughly parallel with the direction of local
616 M_2 tidal energy transport (northward) and it can be assumed that there is little additional total
617 tidal energy to be trapped on the stoss side by the dyke. As a result, the increase of local tidal
618 kinetic energy (shown in Park et al. (2014)) corresponds to a decrease of tidal potential
619 energy, therefore, decreased M_2 tidal amplitude.
620

621

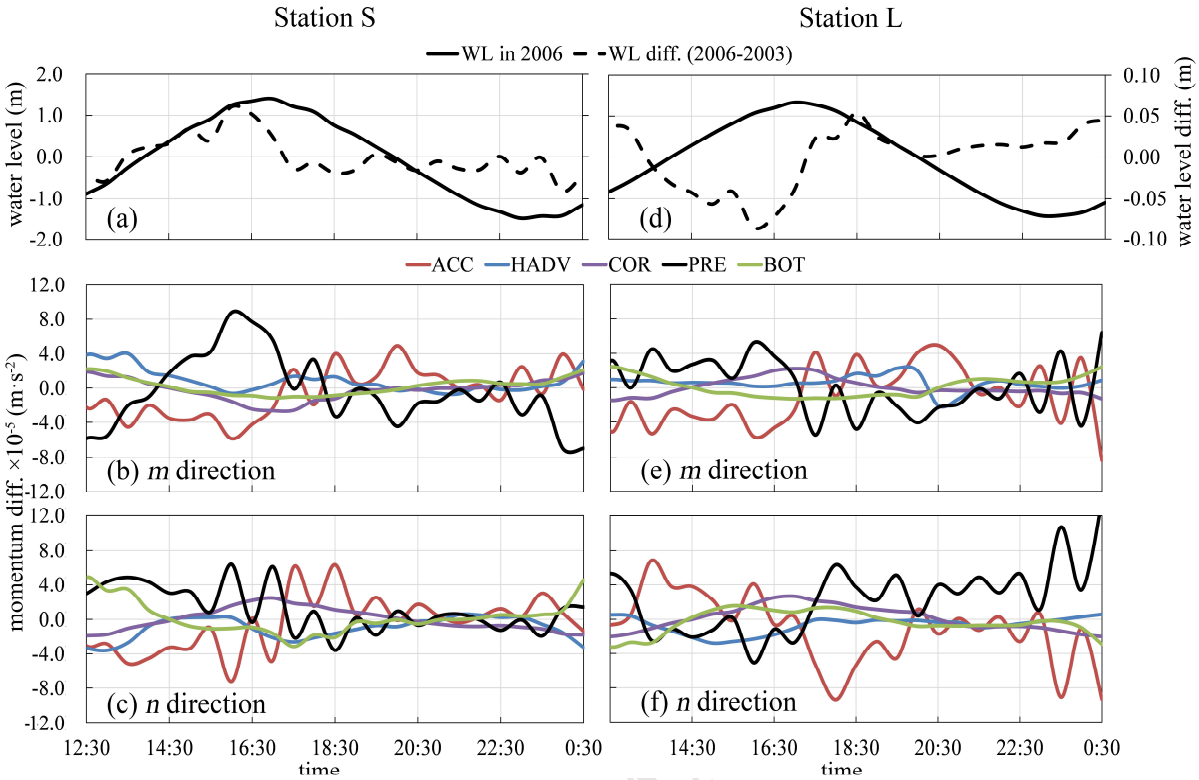

622

623 Fig. 11. Time series of water level in year 2006, and the changes of water level (year
624 2006-2003) and momentum terms (year 2006-2003) due to jetties construction at (a)-(c)
625 stations S and (d)-(f) station L during one tidal cycle (locations of the stations refer to Fig.
626 10j3). The positive direction of momentum term is the same as Fig. 10: ACC (acceleration of
627 tidal current); PRE (pressure gradient); COR (Coriolis force); BOT (bottom friction); HADV
628 (horizontal advection).

629

630

631 **4.2 Shallow-water tide M_4**

632 ***4.2.1 Generation mechanisms***

633 Apart from being distorted by coastal structures, the M_2 tidal wave is subject to the
634 nonlinear self-self interaction, and with other tidal constituents (Gao et al., 2014; Parker,
635 1991; Blanton et al, 2002). As a result, the energetic overtide M_4 is generated by M_2 self-self
636 interaction and the compound tides, e.g. MS_4 and MN_4, are generated by M_2 interaction with
637 semidiurnal S_2 and N_2, respectively. These shallow-water tidal constituents are induced by
638 the fundamental tide through nonlinear terms in continuity and momentum (Gallagher and
639 Munk, 1971; Parker, 1991; Speer and Aubrey, 1985; Song et al., 2016a), which is known as
640 'amplitude dispersive' of shallow-water wave (Speer and Aubrey, 1985). To better estimate
641 the interaction between tidal constituent, we exclude the tidal forcing of M_2 tide (Run 7),
642 shallow-water tides (M_4, MS_4 and MN_4) (Run 8) and other semidiurnal tides (S_2, N_2 and K_2)
643 (Run 9) from the Dalian-Yantai open boundary. As can be seen in Fig. 12, M_4 tide in Run 7 is
644 close to zero after excluding its fundamental M_2 tide, while the spatial distribution of M_4 tide
645 in Run 8 is quite similar to that of the baseline run for 2003 (Fig. 3b). These results imply that
646 the nonlinear overtide M_4 in this shallow-water coast is almost all produced by local M_2
647 self-self interaction, other than energy transport from outside of the basin. Moreover, the
648 relative importance of M_2 to M_4 tide here is greater than other regions (about 70%-80%),
649 probably owing to the shallow bathymetry. With respect to the result of Run 9 (Fig. 12c), as
650 our expectation, the reduction in semidiurnal tides S_2, N_2 and K_2 leads to an enhanced M_4
651 amplitude that is increased onshore by 5 cm. This discrepancy can be explained as: the

nonlinear interactions between M_2 and other semidiurnal tides (S_2, N_2 and K_2) is absent in this situation so that the dissipation by quadratic friction is decreased (Parker, 1991), therefore, an increase of M_2 energy. As a result, there is additional M_2 tidal energy transferred into overtide M_4.

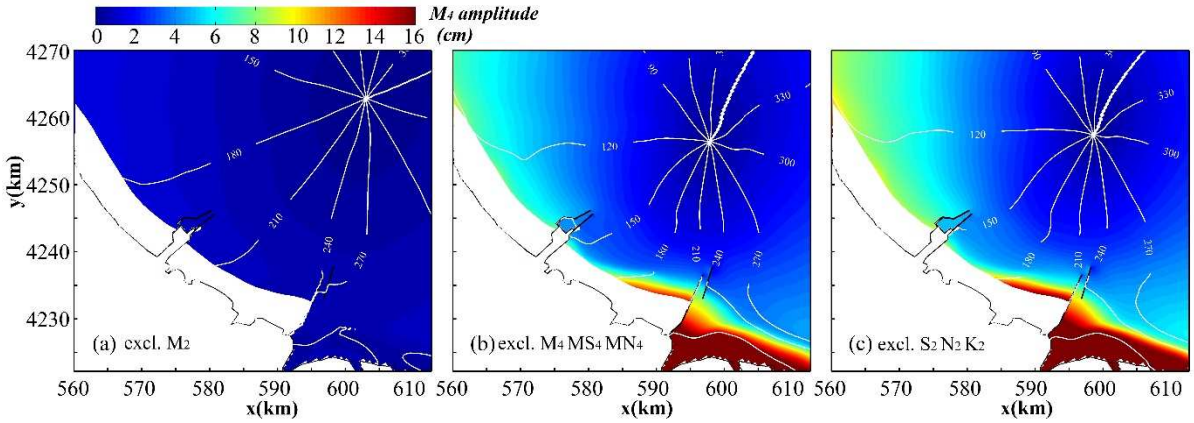

Fig. 12. Tidal amplitude (contour map, unit: cm) and co-phases lines (contour lines, unit: degree) of M_4 tide predicted by model runs excluding (a) M_2 (Run 7), (b) M_4, MS_4 and MN_4 (Run 8) and (c) S_2, N_2 and K_2 (Run 9).

Since M_4 tide is generated locally by M_2 self-self interaction, the spatial structure of M_4 tide is expected to appear a similar pattern to the M_2 one. However, the M_4 tidal amplitude is shown to increase dramatically towards the coast at less than 4 m depth, in particular around the Binzhou Harbor (Fig. 3b, Fig. 12b and 12c), which seems to be inconsistent with M_2 tide (Fig. 3a). In fact, the energy transfer to M_4 not only relates to local M_2 tide but also nonlinearity that is strongly affected by the bottom slope of tidal flat (Li et al., 2018a, 2018b). The water depth shallow than 4 m is then changed to uniform 4 m in Run 10 to evaluate the impact of bottom slope on M_2-M_4 energy transfer. Fig. 13 demonstrates that the coastal M_4 tide is largely in accordance with the M_2 tide, both decrease northeastward, because the uniform water depth has nearly identical nonlinearity at all location, so that energy transfer to

M_4 is in proportion to M_2. However, in the presence of natural slope (Fig. 3b), nonlinearity increases with decreasing water depth towards the shoreline, therefore, more energy is transferred to M_4 towards the shoreline, in particular the shallower eastern Binzhou Harbor.

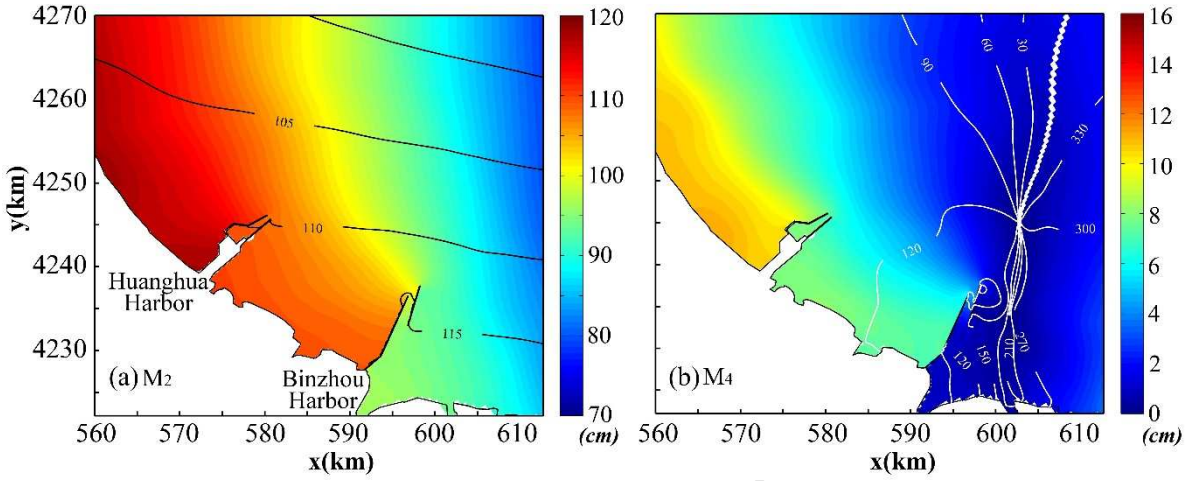

Fig. 13. Tidal amplitude (contour map, unit: cm) and co-phases lines (contour lines, unit: degree) of (a) M_2 tide and (b) M_4 tide for Run 10 with bathymetry shallower than 4 m changed to uniform 4 m.

4.2.2 Effect of nonlinearity change by the structure on M_4

Because overtide M_4 relates to both local M_2 tide and nonlinearity, the discrepancies between the spatial variation of M_2 and M_4 (Fig. 5) are due to the changes in nonlinearity induced by the coastal structure, as shown in Fig. 14. On the stoss side of the jetty, the nonlinear free surface appears to have an arc-shaped variation pattern (Fig. 14a), which corresponds to the spatial distribution of M_4 (marked with red boxes in Fig. 5d). This nonlinearity variation also leads to a larger area of M_4 amplitude change than that of M_2 tide. On the lee side of Huanghua Harbor, the local discrepancy between M_2 and M_4 amplitude change (Fig. 5a and 5d) is generally related to the variation pattern of nonlinear bottom friction (Fig. 14b). It seems like that the bottom friction plays a role in the M_2-M_4 energy

687 transfer on the lee side, in particular in shallow area (Speer and Aubrey, 1985), owing to the
688 remarkable decrease in current velocity. In spite of evident changes around the head of jetties
689 (Fig. 14c), the nonlinear advection has a little effect on changes in energy transfer to M_4 tide.
690 This is likely due to the negligible horizontal advection except for at the head of jetties (as
691 concluded in Section 4.1) where the local M_2 tidal energy is merely about 60% of the coastal
692 one.

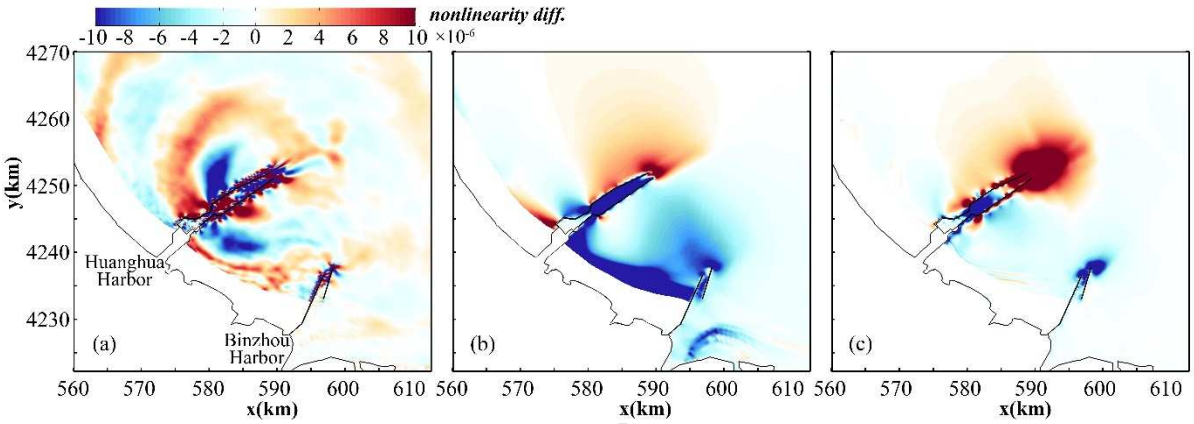

693

694 Fig. 14. Changes in averaged (a) nonlinear free surface (unit: $m \cdot s^{-1}$), (b) bottom friction (unit:
695 $m \cdot s^{-2}$) and (c) horizontal advection (unit: $m \cdot s^{-2}$) between year 2006 and 2003.

696 Overall, tidal nonlinearity are able to result in a distortion of principal tide and generate
697 overtides and compound tides, that is, the nonlinearity can extract tidal energy from low to
698 high frequency tidal components (Gallagher and Munk, 1971; Parker, 1991; Speer and
699 Aubrey, 1985). The above analysis demonstrated that the coastal structures not only cause
700 modification in principal tide but also in nonlinearity, and hence gives rise to the different
701 responses of fundamental tide and its overtide to the structures. Furthermore, the tidal
702 distortion resulted from nonlinearity contributes to an inequal duration of the flood and ebb
703 tide (vertical tide), and the associated inequal strength of the flood an ebb velocities
704 (horizontal tide) (Guo et al., 2019). These inequalities are referred as tidal asymmetry

705 (Dronkers, 1986; Friedrichs and Aubrey, 1988; Guo et al., 2019), whose magnitude is
706 commonly quantified by the ratio of M_2 to M_4 amplitude, and have major effects on sediment
707 transport and morphological evolution (Bertin et al., 2005; Gao et al., 2018; Jewell et al.,
708 2012; Liang et al., 2018; Zarzuelo et al., 2015).

5 Conclusions

In this study, a high resolution Delft3D barotropic tidal model is applied to the Huanghua-Binzhou Harbor, northeastern China to assess the impacts of large-scale sequential harbor constructions (year 2003-2016) on local tidal dynamics. The model results highlight the linkage between tidal modification and changes of momentum and tidal energy, and thus pinpoint the physical mechanism of M_2 tidal distortion by coastal structures. Moreover, the generation and variation of shallow-water tide M_4 is obtained from the energy transfer and nonlinearity.

The tidal dynamics in the study region is governed by a counter-clockwisely rotating M_2 tidal wave, with an amphidromic point at the entrance of Yellow River. Before large-scale constructions of harbors (2003), local tidal energy flux southeasterly alongshore transports with a magnitude of up to 3.0×10^4 $W\cdot m^{-1}$, accompanied with tidal energy density southeasterly decreasing from 5.5 $KJ\cdot m^{-2}$ to 3.0 $KJ\cdot m^{-2}$. However, as the harbors rapidly developed (2006-2016), the transport of tidal energy is strongly impeded and thus results in M_2 tidal amplitude increased on the stoss side and decreased on the lee side of the harbors by 2-6 cm. This interesting feature of M_2 tide is also noticed in other regions globally but is not fully understood. Our model results indicate that this feature is attributed to the following two mechanisms: 1) the obstruction effect of jetty causes tidal energy to be increased and decreased on the stoss side and lee side, respectively, most of which is converted to potential tidal energy; 2) the structure-induced momentum changes in current acceleration is balanced by the pressure gradient. Hence, the alongshore current on the stoss side and cross-shore

current on the lee side are more affected by presence of the harbor structure, which led to a larger tidal range on the stoss side and a smaller tidal range on the lee side, respectively.

In the M_2 dominant region with shallow water depth, nonlinear M_4 tide has an amplitude increasing up to 20 cm towards the coast. The model sensitivity studies indicate that the overtide M_4 is generated locally by M_2 self-self interaction rather than being induced by the tidal energy flux from offshore. This phenomena is in analog to the increased wave harmonics due to wave self-self interaction and therefore wave asymmetry at the low crested breakwater (Zou and Peng, 2011 and Peng et al., 2009). In fact, the M_4 tide is not only related to its fundamental M_2 tide but also associated with local nonlinearity. Our model results suggest that M_4 tide increases towards the shore on the tidal flat with natural slope due to enhanced nonlinearity by decreasing water depth, however, M_4 tide is proportional to M_2 tide on the tidal flat with a constant water depth where local nonlinearity is nearly the same in space. The harbor constructions affect the local nonlinearity and thus the energy transfer from M_2 to M_4, resulting in the discrepancies between changes of M_2 and M_4 tidal amplitude by the jetty built in 2006.

The responses of tide and its nonlinearity to harbor structures are analyzed qualitatively in this study. Further works can be done to quantitatively assess the tidal change and the role of specified nonlinearity. Long-term observations during different construction stages around the coastal structure should be carried out to validate the numerical model. It is a good approximation to use a 2DH barotropic tidal model in this study since the thermohaline stratification in our study region is weak compared to those in the central Bohai Sea and the Bohai Strait (Huang et al., 1999; Liu, 2007; Wang et al., 2010). Nevertheless, future work on

753 the far-field effects of Huanghua-binzhou Harbor in the Bohai Sea should include wind and
754 baroclinicity which have significant impacts on the regional circulation of Bohai Sea (Wang
755 et al., 2010; Wu et al., 2004; Zhou et al., 2017). Consequently, the predicted tidal
756 modification by sequential harbor constructions is likely to have environmental implications
757 (Zhai et al., 2012) and affect the sedimentological process (Qiao et al., 2011), which may lead
758 to responses to coastal structures different from those by the present barotropic model. In
759 addition, bathymetry changes due to sediment transport and morphological evolution may
760 give rise to a change in the local tidal dynamics with a magnitude comparable to those
761 induced by coastal structures (Guo et al., 2018; Pelling et al., 2013), in which case a two way
762 coupled hydrodynamics and morphodynamics model are needed to fully capture the impact
763 of a coastal structure (Peng et al., 2018). During storm events, two way interaction of
764 wave-tide-current-surge needs to be taken into consideration (Song et al., 2016b; Zou and Xie,
765 2016; Zou et al., 2013). Although this study is site-specific, the proposed approach is likely to
766 be applicable to better understand the tidal characteristics change due to changes in geometry
767 and bathymetry and impacts by coastal structures, tidal channel/inlet and river mouth at other
768 sites.

769 ## Acknowledgements

770 This study was supported by the China Geological Survey (Grants
771 No.1212011120087) and National Natural Science Fund of China (Grants No.41776098).
772 The authors would like to thank Dr. Nan Xu (Tsinghua University) for providing the
773 coastline of China. We also thank Associate Editor Professor Sanchez-Arcilla and two
774 anonymous reviewers for their constructive comments.

775

776 ## References

777 Arkema, K.K., Guannel, G., Verutes, G., Wood, S.A., Guerry, A., Ruckelshaus, M., Kareiva,
778 P., Lacayo, M., Silver, J.M., 2013. Coastal habitats shield people and property from
779 sea-level rise and storms. Nature Climate Change. 3 (10), 913-918.

780 Aubrey, D.G., Speer, P.E., 1985. A study of non-linear tidal propagation in shallow inlet
781 estuarine systems .1. Observations. Estuarine, Coastal and Shelf Science. 21 (2),
782 185-205.

783 Bao, X., Gao, G., Yan, J., 2001. Three dimensional simulation of tide and tidal current
784 characteristics in the East China Sea. Oceanologica Acta. 24 (2), 135-149.

785 Bertin, X., Chaumillon, E., Sottolichio, A., Pedreros, R., 2005. Tidal inlet response to
786 sediment infilling of the associated bay and possible implications of human activities: the
787 Marennes-Oléron Bay and the Maumusson Inlet, France. Continental Shelf Research. 25
788 (9), 1115-1131.

789 Blanton, J.O., Lin, G., Elston, S.A., 2002. Tidal current asymmetry in shallow estuaries and
790 tidal creeks. Continental Shelf Research. 22 (11-13), 1731-1743.

791 Blott, S.J., Pye, K., van der Wal, D., Neal, A., 2006. Long-term morphological change and its
792 causes in the Mersey Estuary, NW England. Geomorphology. 81 (1-2), 185-206.

793 Byun, D.S., Wang, X.H., Holloway, P.E., 2004. Tidal characteristic adjustment due to dyke
794 and seawall construction in the Mokpo Coastal Zone, Korea. Estuarine, Coastal and Shelf
795 Science. 59 (2), 185-196.

796 Cheong, S., Silliman, B., Wong, P.P., van Wesenbeeck, B., Kim, C., Guannel, G., 2013.

797 Coastal adaptation with ecological engineering. Nature Climate Change. 3 (9), 787-791.
798 Crain, C.M., Halpern, B.S., Beck, M.W., Kappel, C.V., 2009. Understanding and managing
799 human threats to the coastal marine environment. Annals of the New York Academy of
800 Sciences. 1162 (1), 39-62.
801 Davis, R.A., Barnard, P., 2003. Morphodynamics of the barrier-inlet system, west-central
802 Florida. Marine Geology. 200 (1-4), 77-101.
803 Dai, P., Zhang, J., Zheng, J., 2017. Predictions for dynamic tidal power and associated local
804 hydrodynamic impact in the Taiwan Strait, China. Journal of Coastal Research. 331,
805 149-157.
806 Dai, Z., Liu, J.T., Fu, G., Xie, H., 2013. A thirteen-year record of bathymetric changes in the
807 North Passage, Changjiang (Yangtze) estuary. Geomorphology. 187, 101-107.
808 Dai, Z., Liu, J.T., Wei, W., Chen, J., 2014. Detection of the Three Gorges Dam influence on
809 the Changjiang (Yangtze River) submerged delta. Scientific Reports. 4 (1).
810 Dai, Z., Mei, X., Darby, S.E., Lou, Y., Li, W., 2018. Fluvial sediment transfer in the
811 Changjiang (Yangtze) river-estuary depositional system. Journal of Hydrology. 566,
812 719-734.
813 Dyer, K. R., 1973. Estuaries: A Physical Introduction. Wiley, London, 140 (74).
814 Deltares, 2013. Delft3D-FLOW User Manual, 3.15.30808 ed. Deltares, Delft.
815 Ding, Y., Wei, H., 2017. Modeling the impact of land reclamation on storm surges in Bohai
816 Sea, China. Natural Hazards. 85 (1), 559-573.
817 Dronkers, J., 1986. Tidal asymmetry and estuarine morphology. Netherlands Journal of Sea
818 Research. 20 (2-3), 117-131.

819 Fang, G., Wang, Y.G., Wei, Z.X., Choi, B.H, Wang, X.Y., Wang, J., 2004. Empirical cotidal
820 charts of the Bohai, Yellow, and East China Seas from 10 years of TOPEX/Poseidon
821 altimetry. Journal of Geophysical Research. 109 (C11).
822 Feng, X., Li J., Hao, P., Li, J., Zhang, H., 2008. Relation between sudden sedimentation and
823 wind energy in outer channel of Huanghua Port and its application in Binzhou Port.
824 China Ocean Engineering. (1), 161-170.
825 Foreman, M.G.G., Henry, R.F., Walters, R.A., Ballantyne, V.A., 1993. A finite element
826 model for tides and resonance along the north coast of British Columbia. Journal of
827 Geophysical Research: Oceans. 98 (C2), 2509-2531.
828 Friedrichs, C.T., Aubrey, D.G., 1988. Non-linear tidal distortion in shallow well-mixed
829 estuaries – a synthesis. Estuarine Coastal and Shelf Science. 27 (5), 521-545.
830 Gallagher B S, Munk, W.H., 1971. Tides in shallow water: Spectroscopy. Tellus. 23 (4-5),
831 346-363.
832 Gao, G.D., Wang, X.H., Bao, X.W., 2014. Land reclamation and its impact on tidal dynamics
833 in Jiaozhou Bay, Qingdao, China. Estuarine, Coastal and Shelf Science. 151, 285-294.
834 Gao, G.D., Wang, X.H., Bao, X.W., Song, D., Lin, X.P., Qiao, L.L., 2018. The impacts of
835 land reclamation on suspended-sediment dynamics in Jiaozhou Bay, Qingdao, China.
836 Estuarine, Coastal and Shelf Science. 206, 61-75.
837 Guo, W., Wang, X.H., Ding, P., Ge, J., Song, D., 2018. A system shift in tidal choking due to
838 the construction of Yangshan Harbour, Shanghai, China. Estuarine, Coastal and Shelf
839 Science. 206, 49-60.
840 Guo, L., Wang, Z.B., Townend, I., He, Q., 2019. Quantification of tidal asymmetry and its

841 nonstationary variations. Journal of Geophysical Research: Oceans. 124 (1), 773-787.

842 Hou, Q.Z., 2013. Study for impacts of contiguous development in Bohai Bay on coastal
843 mudflat hydraulic environment and evolution process (in Chinese). Ph.D. Thesis. Nanjing
844 Normal University, Nanjing, China.

845 He, Y., Lu, X., Qiu, Z., Zhao, J., 2004. Shallow water tidal constituents in the Bohai Sea and
846 the Yellow Sea from a numerical adjoint model with TOPEX/POSEIDON altimeter data.
847 Continental Shelf Research. 24 (13-14), 1521-1529.

848 Hench, J.L., Luettich, R.A., 2003. Transient tidal circulation and momentum balances at a
849 shallow inlet. Journal of Physical Oceanography. 33 (4), 913-932.

850 Hu K.L., Ding P.X., Wang Z.B., Yang S.L., 2009. A 2D/3D hydrodynamic and sediment
851 transport model for the Yangtze Estuary, China. Journal of Marine Systems. 77(1-2),
852 114-136.

853 Huang, D., Su, J., Backhaus, J.O., 1999. Modelling the seasonal thermal stratification and
854 baroclinic circulation in the Bohai Sea. Continental Shelf Research. 19 (11), 1485-1505.

855 Jewell, S.A., Walker, D.J., Fortunato, A.B., 2012. Tidal asymmetry in a coastal lagoon
856 subject to a mixed tidal regime. Geomorphology. 138 (1), 171-180.

857 Jia, H., Shen, Y., Su, M., Yu, C., 2018. Numerical simulation of hydrodynamic and water
858 quality effects of shoreline changes in Bohai Bay. Frontiers of Earth Science. 12 (3),
859 625-639.

860 Kuang, C., Mao, X., Liu, P., Deng, L., Gu, J., Ma, Z., Du, D., Yang, J., Liu, F., Song, H.,
861 2015. Influence of wind force on a silt-muddy coast: Huanghua Harbor coast, China.
862 Journal of Waterway Port Coastal and Ocean Engineering. 141 (050150016).

863 Lee, S., Lie, H., Song, K., Cho, C., Lim, E., 2008. Tidal modification and its effect on
864 sluice-gate outflow after completion of the Saemangeum dike, South Korea. Journal of
865 Oceanography. 64 (5), 763-776.
866 Lee J.H.W., Qu B., 2004. Hydrodynamic tracking of the massive spring 1998 red tide in
867 Hong Kong. Journal of Environmental Engineering. 130(5), 535-550.
868 Lefèvre, F., Le Provost, C., Lyard, F.H., 2000. How can we improve a global ocean tide
869 model at a regional scale? A test on the Yellow Sea and the East China Sea. Journal of
870 Geophysical Research: Oceans. 105 (C4), 8707-8725.
871 Lesser, G.R., Roelvink, J.A., van Kester, J.A.T.M., Stelling, G.S., 2004. Development and
872 validation of a three-dimensional morphological model. Coastal Engineering. 51 (8-9),
873 883-915.
874 Li, K., Liu, X., Zhao, X., Guo, W., 2010. Effects of reclamation projects on marine ecological
875 environment in Tianjin Harbor industrial zone. Procedia Environmental Sciences. 2,
876 792-799.
877 Li, L., Wang, X.H., Williams, D., Sidhu, H., Song, D., 2012. Numerical study of the effects
878 of mangrove areas and tidal flats on tides: A case study of Darwin Harbour, Australia.
879 Journal of Geophysical Research: Oceans. 117 (C06011).
880 Li, L., Guan, W., He, Z., Yao, Y., Xia, Y., 2017. Responses of water environment to tidal flat
881 reduction in Xiangshan Bay: Part II locally re-suspended sediment dynamics. Estuarine,
882 Coastal and Shelf Science. 198, 114-127.
883 Li, L., Guan, W., Hu, J., Cheng, P., Wang, X.H., 2018a. Responses of water environment to
884 tidal flat reduction in Xiangshan Bay: Part I hydrodynamics. Estuarine, Coastal and Shelf

885 Science. 206, 14-26.

886 Li, L., Ye, T., He, Z., Xia, Y., 2018b. A numerical study on the effect of tidal flat's slope on
887 tidal dynamics in the Xiangshan Bay, China. Acta Oceanologica Sinica. 37 (9), 29-40.

888 Liang, H., Kuang, C., Olabarrieta, M., Song, H., Ma, Y., Dong, Z., Han, X., Zuo, L., Liu, Y.,
889 2018. Morphodynamic responses of Caofeidian channel-shoal system to sequential
890 large-scale land reclamation. Continental Shelf Research. 165, 12-25.

891 Liu, H., 2007. Annual cycle of stratification and tidal fronts in the Bohai Sea: A model study.
892 Journal of Oceanography. 63 (1), 67-75.

893 Lu, Y., Ji, R., Zuo, L., 2009. Morphodynamic responses to the deep water harbor
894 development in the Caofeidian sea area, China's Bohai Bay. Coastal Engineering. 56 (8),
895 831-843.

896 Mulder, J.P.M., Louters, T., 1994. Changes in basin geomorphology after implementation of
897 the Oosterschelde estuary project. Hydrobiologia. 282-283 (1), 29-39.

898 Parker, B. B., 1991. The Relative Importance of the Various Nonlinear Mechanisms in a
899 Wide Range of Tidal Interaction (Review), Tidal hydrodynamics. Wiley, New York,
900 237-268.

901 Park, Y., Kim, H., Hwang, J.H., Kim, T., Park, S., Nam, J., Seo, Y., 2014. Dynamics of dike
902 effects on tidal circulation around Saemangeum, Korea. Ocean & Coastal Management.
903 102, 572-582.

904 Pawlowicz, R., Beardsley, B., Lentz, S., 2002. Classical tidal harmonic analysis including
905 error estimates in MATLAB using T_TIDE. Computers and Geosciences. 28 (8),
906 929-937.

907 Pelling, H.E., Uehara, K., Green, J.A.M., 2013. The impact of rapid coastline changes and
908 sea level rise on the tides in the Bohai Sea, China. Journal of Geophysical Research:
909 Oceans. 118 (7), 3462-3472.
910 Peng, Z., Zou, Q.P., Reeve, D., Wang, B., 2009. Parameterisation and transformation of wave
911 asymmetries over a low-crested breakwater. Coastal Engineering. 56 (11-12), 1123-1132.
912 Peng, Z., Zou, Q.P., Lin, P., 2018. A partial cell technique for modeling the morphological
913 change and scour. Coastal Engineering, 131, 88-105.
914 Pingree, R.D., Maddock, L., 1978. M4 tide in english-channel derived from a nonlinear
915 numerical-model of M2 tide. Deep-Sea Research. 25 (1), 53-63.
916 Qiao, L.L., Wang, Y.Z., Li, G.X., Deng, S.G., Liu, Y., Mu, L., 2011. Distribution of
917 suspended particulate matter in the northern Bohai Bay in summer and its relation with
918 thermocline. Estuarine, Coastal and Shelf Science. 93 (3), 212-219.
919 Sheng, J., Wang, L., 2004. Numerical study of tidal circulation and nonlinear dynamics in
920 Lunenburg Bay, Nova Scotia. Journal of Geophysical Research. 109 (C10).
921 Song, D., Wang, X.H., Zhu, X., Bao, X., 2013. Modeling studies of the far-field effects of
922 tidal flat reclamation on tidal dynamics in the East China Seas. Estuarine, Coastal and
923 Shelf Science. 133, 147-160.
924 Song, D., Yan, Y., Wu, W., Diao, X., Ding, Y., Bao, X., 2016a. Tidal distortion caused by the
925 resonance of sexta-diurnal tides in a micromesotidal embayment. Journal of Geophysical
926 Research: Oceans. 121 (10), 7599-7618.
927 Song, H., Kuang, C., Liang, H., Gu, J., 2016b. Numerical modeling of current and wave
928 interaction in Huanghua Harbor, China, The Twelfth ISOPE Pacific/Asia Offshore

Mechanics Symposium, Gold Coast.

Song, H., Kuang, C., Liang, H., Xie, H., 2017. Impacts of construction of harbor projects on hydrodynamic and sediment transport enviroments in the southwest of Bohai Bay (in Chinese). Journal of Tongji University (Natural Science). 45 (04), 511-518.

Speer, P.E., Aubrey, D.G., 1985. A study of non-linear tidal propagation in shallow inlet estuarine systems .2. Theory. Estuarine Coastal and Shelf Science. 21 (2), 207-224.

Suh, S.W., Lee, H.Y., Kim, H.J., 2014. Spatio-temporal variability of tidal asymmetry due to multiple coastal constructions along the west coast of Korea. Estuarine, Coastal and Shelf Science. 151, 336-346.

Tian, B., Wu, W., Yang, Z., Zhou, Y., 2016. Drivers, trends, and potential impacts of long-term coastal reclamation in China from 1985 to 2010. Estuarine Coastal and Shelf Science. 170, 83-90.

Turner, R.K., Subak, S., Adger, W.N., 1996. Pressures, trends, and impacts in coastal zones: Interactions between socioeconomic and natural systems. Environmental Management. 20 (2), 159-173.

Van der Wegen, M., Roelvink, J.A., 2012. Reproduction of estuarine bathymetry by means of a process-based model: Western Scheldt case study, the Netherlands. Geomorphology. 179, 152-167.

Van Maren, D. S., Van Kessel, T., Cronin, K., Sittoni, L., 2015. The impact of channel deepening and dredging on estuarine sediment concentration. Continental Shelf Research. 95, 1-14.

Vousdoukas, M.I., Voukouvalas, E., Annunziato, A., Giardino, A., Feyen, L., 2016.

951 Projections of extreme storm surge levels along Europe. Climate Dynamics. 47 (9-10),
952 3171-3190.
953 Wang, Y.P., Gao, S., Jia, J., Thompson, C.E.L., Gao, J., Yang, Y., 2012. Sediment transport
954 over an accretional intertidal flat with influences of reclamation, Jiangsu coast, China.
955 Marine Geology. 291-294, 147-161.
956 Wang, Y., Tang, L., Wang, C., Liu, C., Dong, Z., 2014. Combined effects of channel
957 dredging, land reclamation and long-range jetties upon the long-term evolution of
958 channel-shoal system in Qinzhou bay, SW China. Ocean Engineering. 91, 340-349.
959 Wang, J., Shen, Y., Guo, Y., 2010. Seasonal circulation and influence factors of the Bohai
960 Sea: a numerical study based on Lagrangian particle tracking method. Ocean Dynamics.
961 60 (6), 1581-1596.
962 Wu, R., Jiang, Z., Li, C., 2018. Revisiting the tidal dynamics in the complex Zhoushan
963 Archipelago waters: A numerical experiment. Ocean Modelling. 132, 139-156.
964 Wu, D., Wan, X., Bao, X., Mu, L., Lan, J., 2004. Comparison of summer thermohaline field
965 and circulation structure of the Bohai Sea between 1958 and 2000. Chinese Science
966 Bulletin. 49 (4), 363.
967 Xie, L.S., Hsieh, W.W., Helbig, J.A., 1990. A tidal model of Bohai. Continental Shelf
968 Research. 10 (8), 707-721.
969 Xu, N., Gong, P., 2018. Significant coastline changes in China during 1991 – 2015 tracked by
970 Landsat data. Science Bulletin. 63 (14), 883-886.
971 Zarzuelo, C., Díez-Minguito, M., Ortega-Sánchez, M., López-Ruiz, A., Losada, M.Á., 2015.
972 Hydrodynamics response to planned human interventions in a highly altered embayment:

973 The example of the Bay of Cádiz (Spain). Estuarine, Coastal and Shelf Science. 167,
974 75-85.
975 Zhai, W., Zhao, H., Zheng, N., Xu, Y., 2012. Coastal acidification in summer bottom
976 oxygen-depleted waters in northwestern-northern Bohai Sea from June to August in 2011.
977 Chinese Science Bulletin. 57 (9), 1062-1068.
978 Zhu, L., Hu, R., Zhu, H., Jiang, S., Xu, Y., Wang, N., 2018. Modeling studies of tidal
979 dynamics and the associated responses to coastline changes in the Bohai Sea, China.
980 Ocean Dynamics. 68 (12), 1625-1648.
981 Zhu, Z., Zhu, X., Guo, X., 2017. Coastal tomographic mapping of nonlinear tidal currents and
982 residual currents. Continental Shelf Research. 143, 219-227.
983 Zhou, F., Huang, D., Xue, H., Xuan, J., Yan, T., Ni, X., Zeng, D., Li, J., 2017. Circulations
984 associated with cold pools in the Bohai Sea on the Chinese continental shelf. Continental
985 Shelf Research. 137, 25-38.
986 Zou, Q.P., Peng, Z., 2011. Evolution of wave shape over a low-crested structure. Coastal
987 Engineering. 58 (6), 478-488.
988 Zou, Q.P., Xie, D., 2016. Tide-surge and wave interaction in the Gulf of Maine during an
989 extratropical storm. Ocean Dynamics. 66 (12), 1715-1732.
990 Zou, Q. P., Chen, Y., Cluckie, I., Hewston, R., Pan, S., Peng, Z., Reeve, D., 2013. Ensemble
991 prediction of coastal flood risk arising from overtopping by linking meteorological, ocean,
992 coastal and surf zone models. Quarterly Journal of the Royal Meteorological Society,
993 139(671), 298-313.

Highlights:

- Numerically investigate the tidal dynamics changes induced by the large-scale sequential constructions.
- Predominant M_2 tide increased on the stoss side and decreased on the lee side of the harbor jetties.
- Structure-induced changes in current acceleration is balanced by the changes in pressure gradient.
- M_4 tide is generated locally by M_2 self-self interaction, which is relative to M_2 tidal energy and local nonlinearity.
- Three prominent separated bands of tidal energy density appear in the third harbor construction phase.